

# Numerically refined reaction conditions for stochastic simulation of nonelementary trimolecular reactions between closest particles

Taylor Kearney,<sup>1,\*</sup> Ricardo Ruiz-Baier<sup>1,2,3,†</sup> and Mark B. Flegg<sup>1,‡</sup>

<sup>1</sup>*School of Mathematics, Monash University, 9 Rainforest walk, 3800 Clayton, Victoria, Australia*

<sup>2</sup>*Universidad Adventista de Chile, Casilla 7-D Chillán, Chile*

<sup>3</sup>*Institute for Computer Science and Mathematical Modeling, Sechenov First Moscow State Medical University, Moscow, Russia*



(Received 20 April 2025; revised 31 July 2025; accepted 5 August 2025; published 22 September 2025)

We study a system of diffusing point particles in which any triplet of particles reacts and is removed from the system when the relative proximity of the constituent particles satisfies a predefined condition. Proximity-based reaction conditions of this kind are commonly used in particle-based simulations of chemical kinetics to mimic bimolecular reactions (those involving just two reactants) and have been extensively studied. The rate at which particles react within the system is determined by the reaction condition and particulate diffusion. In the bimolecular case, analytic relations exist between the reaction rate and the distance at which particles react allowing modellers to tune the rate of the reaction within their simulations by simply altering the reaction condition. However, generalizing proximity-based reaction conditions to trimolecular reactions (those involving three particles) is more complicated because it requires understanding the distribution of the closest diffusing particle to a point in the vicinity of a spatially dependent absorbing boundary condition. We find that in this case the evolution of the system is described by a nonlinear partial integrodifferential equation with no known analytic solution, which makes it difficult to relate the reaction rate to the reaction condition. To resolve this, we use singular perturbation theory to obtain a leading-order solution and show how to derive an approximate expression for the reaction rate. We then use finite-element methods to quantify the higher-order corrections to this solution and the reaction rate, which are difficult to obtain analytically. Leveraging the insights gathered from this analysis, we demonstrate how to correct for the errors that arise from adopting the approximate expression for the reaction rate, enabling for the construction of more accurate particle-based simulations than previously possible.

DOI: [10.1103/gd4f-nyqv](https://doi.org/10.1103/gd4f-nyqv)

## I. INTRODUCTION

Transport-dependent phenomena are ubiquitous in many chemical systems, particularly in intracellular environments. The most fundamental example of molecular transport is the thermally driven random motion that results in a net movement from regions of high concentration to those with lower concentrations, known as diffusion [1]. Due to its fundamental nature, diffusion is both ubiquitous and essential in biology [2]. It plays a central role in the operation of microorganisms [3] and is vital in numerous cellular processes, including metabolism [4,5] and signaling [6–8]. More broadly, diffusion facilitates the mixing of reactants on small spatial scales, promoting the molecular collisions necessary for biochemical reactions to occur [9,10]. If reactant diffusion is sufficiently slow, then it largely determines the reaction rate, leading to a *diffusion-limited* reaction. This has driven significant interest in diffusion-limited reactions and their kinetics have been extensively studied at various levels of fidelity.

Many models consider the kinetics of diffusion-limited reactions to be deterministic, assuming that the reactants can be well approximated using continuous concentrations. These deterministic models use either ordinary differential equations to investigate only the temporal evolution of reactant concentrations [11,12] or employ partial differential equations (PDEs), known as reaction-diffusion equations, to explicitly incorporate reactant diffusion [13,14]. Although such models have been widely studied, they provide an inadequate description of many biological systems whose kinetics are inherently stochastic [15–18] due to their molecular origins. Moreover, molecular populations are often so low or so spatially localized that meaningful concentrations cannot be defined [19,20].

These shortcomings have motivated the development of a range of models, summarized in Fig. 1 and reviewed in Ref. [21], that incorporate stochastic effects as a core component. The chemical master equation (CME) [22,23] is one of the earliest and most influential models in this class. It is a system of coupled ordinary differential equations that describes the time evolution of the probability mass function for the system to contain a specific number of molecules of each species at time  $t$ . In general, the CME is very difficult to solve analytically [24] and so the stochastic time evolution of molecular populations is typically simulated using Gillespie's

\*Contact author: [taylor. Kearney1@monash.edu](mailto:taylor. Kearney1@monash.edu)

†Contact author: [ricardo.ruizbaier@monash.edu](mailto:ricardo.ruizbaier@monash.edu)

‡Contact author: [mark.flegg@monash.edu](mailto:mark.flegg@monash.edu)

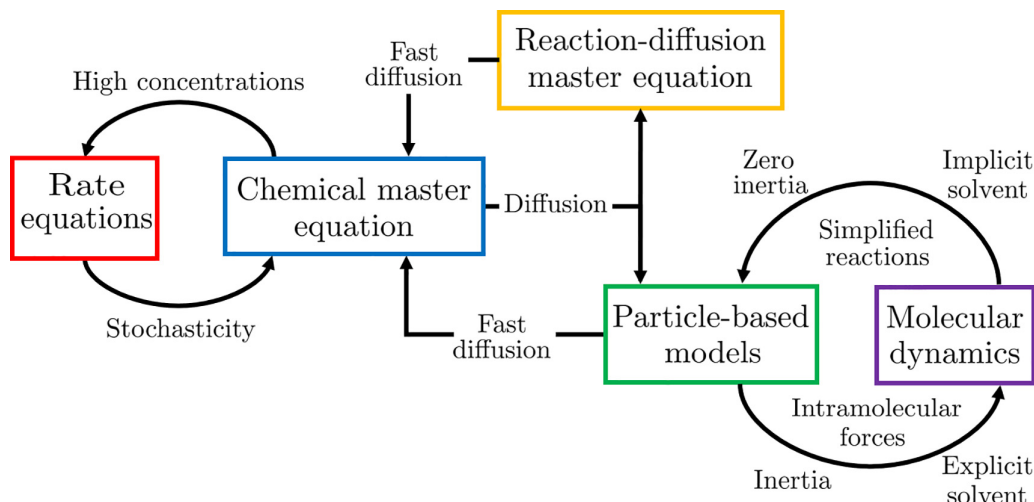


FIG. 1. A summary of the relationships between models of biochemical reactions. The models increase in complexity and physical realism from left to right. The rightward arrows indicate the additional physical mechanisms required to progress to a more detailed model. Conversely, the leftward arrows represent the limit in which a more complicated model reduces to a simpler one. Particle-based models are obtained from molecular dynamics models by assuming reactants undergo diffusive motion as a result of their collisions with implicit solvent molecules and replacing complicated intramolecular interactions with simplified reaction conditions. Particle-based models are an alternative to the reaction-diffusion master equation (RDME) in that they account for reactant diffusion neglected by the chemical master equation (CME). This figure was adapted from Ref. [21] which provides a detailed review of the relationships summarized here.

stochastic simulation algorithm (SSA) [25,26]. The CME, and hence the SSA, applies only to spatially homogeneous, or well-mixed chemical systems, but it can be extended to spatially heterogeneous systems by dividing the domain into spatially homogeneous voxels or compartments that are coupled through diffusive transfers [27,28].

This approach leads to a model commonly referred to as the reaction-diffusion master equation (RDME) [29], which discretizes space in the same manner but does not necessarily rely on the SSA to evolve voxel populations [30–34]. The RDME provides a computationally efficient way to incorporate spatial dependence in stochastic models. However, the size of the voxels is inherently limited by the assumption that they are well mixed. In many cases, finer spatial resolution is required to accurately capture the behavior of the system, leading to more computationally intensive RDME approaches [35].

Perhaps the most natural choice for models of reaction-diffusion systems are those that aim to faithfully replicate the actual dynamics of the system by explicitly treating molecules as individuals undergoing a reaction-diffusion process. Molecular dynamics simulations [36] take this notion to the extreme, attempting to accurately reproduce the physical system with atomic detail. Although they are highly accurate, these simulations can be prohibitively expensive due to the sheer number of degrees of freedom that must be modelled; many of which arise from the need to explicitly track solvent molecules, account for numerous possible interactions, and capture intramolecular timescales [37].

To partially mitigate these computational challenges, particle-based models leverage simplifying assumptions to improve efficiency [21,38] and are widely used in the literature [39]. These models avoid the explicit treatment of solvent molecules and describe the relevant reactants as points undergoing isotropic diffusion on a continuous domain. In

the absence of spatial morphology for individual molecules, these approaches typically favor idealized proximity-based (and sometimes energy-potential-based) reaction conditions that are simple to implement, making such simulations feasible to run on personal computing hardware.

This approach was largely inspired by Smoluchowski [40], who postulated that bimolecular reactions could be modelled by assuming that two molecules undergo a reaction if they come within a predefined distance  $\sigma$ , called the *reaction radius*. Although simple, Smoluchowski’s reaction condition has proven remarkably robust and forms the basis of many prominent software packages for particle-based simulation of reaction-diffusion systems, including Green’s function reaction dynamics [41,42], enhanced Green’s function reaction dynamics [43,44], Smoldyn [45], and ReaDDy [46].

For a bimolecular reaction between two chemical species A and B, Smoluchowski’s model imposes that the rate of reaction is simply the number of successful “collisions” between molecules of A and B at a distance  $\sigma$  per unit time. This reaction rate is inherently stochastic because it depends on the motion of individual diffusing molecules. However, if we were to average the reaction rates obtained from a large ensemble of independent molecules of A surrounded by molecules of B, then the expected reaction rate should converge to the corresponding macroscopic rate. This provides a matching condition that can be used to determine the currently unknown reaction radius  $\sigma$ .

To derive this condition, we consider a system of extremely large (relative to molecular sizes) volume  $V$  that contains a single isolated molecule of A surrounded by molecules of B. For this system, the joint probability density  $P_S(r_1, t)$  for finding a molecule of B, that has never collided with A, at a given position at time  $t$  only depends on the radial distance  $r_1$  between this molecule and A and evolves according to the

diffusion equation,

$$\frac{dP_S(r_1, t)}{dt} = \frac{\hat{D}_1}{r_1^2} \frac{\partial}{\partial r_1} \left( r_1^2 \frac{\partial P_S(r_1, t)}{\partial r_1} \right), \quad (1.1)$$

where  $\hat{D}_1 = D_0 + D_1$  is the relative diffusion coefficient between molecules A and B (the sum of their diffusion coefficients). Smoluchowski's reaction condition specifies that molecules of B must be removed from the system at a distance  $r_1 = \sigma$  from A which manifests as an absorbing boundary condition,

$$P_S(r_1, t) = 0 \text{ on } r_1 = \sigma. \quad (1.2)$$

The expected reaction rate is given by the diffusive flux over this boundary which rapidly approaches the pseudoequilibrium value [40,47],

$$K_S(\sigma) = \frac{k_2}{V} = \frac{4\pi\sigma\hat{D}_1}{V}, \quad (1.3)$$

where  $k_2$  is the bimolecular rate of reaction (first passage rate for a collision). Notice that Eq. (1.3) assumes that

$$\lim_{r_1 \rightarrow \infty} P_S(r_1, t) = \frac{1}{V}. \quad (1.4)$$

This requires that the molecules of B are initially well mixed (distributed uniformly at random) and that the absorption of molecules on  $r_1 = \sigma$  does not perturb the probability density far from this boundary.

Equation (1.3) gives the reaction rate for a single molecule of A per molecule of B and is used to determine  $\sigma$  based on a known second-order rate constant  $k_2$ . To recover the macroscopic reaction rate we assume that molecules of A can be considered independently, so that the expected reaction rate for a system containing multiple molecules is given by Eq. (1.3) multiplied the number of molecules of A and the number of molecules of B. Note that often Eq. (1.3) is instead multiplied by the concentration of A (rather than the number of A molecules), since for an elementary bimolecular reaction the resulting rate of change for the concentration can be directly compared to the macroscopic rate given by the law of mass action, which states the rate is given by the product of the reactant concentrations multiplied by the second-order rate constant  $k_2$  associated with the reaction.

The validity of Smoluchowski's reaction condition, and the many derivatives it has inspired [20,48,49], is contingent upon the distance at which molecules interact being sufficiently small. Specifically, for Smoluchowski's model, the reaction radius  $\sigma$  must be sufficiently small when compared to the expected separation between the molecules [50]. In other words, we require the system to be sufficiently sparse or the affinity of A for B to be sufficiently low so that the associated reaction radius is small. Collins and Kimball [48] alleviate this requirement by supposing that not every collision results in a reaction which amounts to replacing Smoluchowski's absorbing boundary in Eq. (1.2) with a partially reflective condition. Similarly, Doi [49] allows reactants to approach arbitrarily close to each other and only requires that reactions occur at a fixed rate per unit time once reactants are separated by a distance less than the analogous reaction radius parameter. These alternative reaction conditions enable the distance at

which molecules react to be increased for a fixed reaction rate when compared to Smoluchowski's reaction condition, but in each case the reaction condition is still fundamentally a proximity-dependent interaction between molecules that can be summarized by a single parameter, analogously to  $\sigma$ , which determines the spatial scale at which interactions occur [51]. Moreover, for our assumptions regarding the independence of reactants of the same species to be accurate, the interaction distance must still be small regardless of the reaction condition adopted.

Flegg [51] demonstrated that proximity-based reaction conditions equivalent to Smoluchowski's can also be applied to higher-order reactions (those involving more than two reactants), while Kearney and Flegg [50] demonstrated proximity-based trimolecular reaction conditions can produce *nonelementary* kinetics that cannot be described by the law of mass action. In this article, we consider a trimolecular reaction of the general form



which we suppose is mediated by a proximity-based reaction condition akin to those developed by Kearney and Flegg [50].

To describe the reaction condition, we follow Flegg [51] and generalize the notion of reactant proximity to trimolecular reactions by introducing two new coordinates,  $\eta_1$  and  $\eta_2$ . We will discuss this coordinate system in greater detail in Sec. II, so for now it is sufficient to note that  $\eta_1$  describes the separation between a particular pair of A and B molecules. While  $\eta_2$  captures the relative proximity of a third molecule C to this pair. Due to the radial symmetry of the system, proximity-based reaction conditions for the reaction in Eq. (1.5) can be expressed naturally as functions of the radial coordinates  $r_i \equiv ||\eta_i||$ . Smoluchowski's original bimolecular condition can be extended in a straightforward manner to our trimolecular reaction by considering a reaction boundary that extends only a small distance in both  $r_1$  and  $r_2$ . In this case, the system will reach a pseudoequilibrium that returns trimolecular mass-action kinetics. However, a trimolecular system contains an additional spatial degree of freedom, namely  $r_2$ , when compared to a bimolecular system, which offers an opportunity to consider more elaborate reaction conditions. Specifically, we can consider reaction conditions where the separation,  $r_1$ , at which the pair of A and B molecules reacts is mediated by the distance,  $r_2$ , to the molecule of C that is closest to this pair. In this case, the reaction condition still manifests as an absorbing boundary  $\partial\Omega_R$  that is always small in the  $\eta_1$  direction, meaning molecules of A and B must be close if they are to react but now can be comparatively long in the  $\eta_2$  direction so the molecule of C involved in the reaction is not necessarily close to A and B.

The expected reaction rate for the trimolecular system is calculated in the same way as it is for a bimolecular system and is determined by the total flux of the probability density across  $\partial\Omega_R$ . However, now we are concerned with the probability density for finding the state, where each state consists of the pair of A and B molecules and a particular molecule of C, associated with the C molecule with the minimum  $r_2$  value. That is, we must restrict our attention to the state that contains the molecule of C that is closest to A and B, since this state will be the first to satisfy the reaction condition. For all but the

simplest choices of  $\partial\Omega_R$ , determining this probability density analytically is very difficult, and thus it is not possible to derive an analytic expression for the reaction rate in general. To avoid this issue, Kearney and Flegg [50] (implicitly) utilized singular perturbation theory to derive a leading-order solution for the steady-state probability density near  $\partial\Omega_R$ . They then demonstrated, via a particle-based simulation, that the total flux across this boundary can be approximated by just the diffusive flux of this leading-order solution in the  $\eta_1$  direction. This approximation yields an analytic expression, analogous to Smoluchowski's in Eq. (1.3), which relates the reaction rate to the reaction boundary and thus allows us to match  $\partial\Omega_R$  to any given reaction rate.

Unfortunately, this approximation will yield a reaction boundary that does not exactly reproduce the desired reaction rate when incorporated into a simulation, and instead small errors are observed between the simulated and desired rates. These errors are the result of neglecting second-order contributions to the diffusive flux in the  $\eta_1$  direction across  $\partial\Omega_R$  and entirely neglecting the flux across this boundary in the  $\eta_2$  direction that arises from the relative motion of C molecules. That is, the simulated rate reflects the exact flux across  $\partial\Omega_R$  which in general differs from what we are led to expect when adopting the approximate reaction rate. In this article, we seek to address these shortcomings by examining the accuracy of this approximation for the functional form of  $\partial\Omega_R$  considered by Kearney and Flegg [50].

We begin in Sec. II by deriving a nonlinear partial integrodifferential equation that governs the evolution of the probability density to find the state associated with the closest molecule of C and whose analytic solution is unknown for arbitrary  $\partial\Omega_R$ . Although we consider its direct application to the optimization of particle-based simulations, this equation has broader interest in applied mathematics. This work is, in part, a continuation of Redner and Ben-Avraham's [52] in which they examined the distance of the closest molecule to a static trap. Redner and Ben-Avraham generalized the three-dimensional Hertz distribution [53], which assumes that both the trap and surrounding molecules are static, but only considered a constant reaction radius. In contrast, we consider the case where this radius varies with  $r_2$ . Moreover, since all reactants undergo diffusion it is tempting to compare our results to the case where the trap is also mobile, which has been studied in lower-dimensional systems [54,55]; however, such studies are typically concerned with the correlations that arise between reactants [56–58], whereas we restrict our attention to the mean-field behavior of the system.

We use singular perturbation theory [59,60] to derive a leading-order solution for the probability density to find the closest molecule and demonstrate how to use this solution to construct the aforementioned approximation to the steady-state reaction rate. Ideally, we would continue with this analysis to derive the higher-order corrections to the solution, and hence to the reaction rate, but the particular form of the problem makes this challenging. Thus, to quantify these corrections we turn to numerical methods, which are the other “principal approach for solving singular perturbation problems” [59] and are commonly used to investigate singularly perturbed reaction-diffusion systems [61–63]. Since both the probability density and the flux of this quantity are of interest,

in Sec. III we adopt a mixed-primal variational formulation of the problem and present the corresponding finite-element discretization, which uses a continuous interior penalty scheme for the primal equation. The associated finite-element solutions are then used to probe the higher-order corrections to the probability density and the reaction rate in Sec. IV A. Finally, in Sec. IV B we demonstrate how to alter the reaction boundary so that it more accurately reproduces the desired reaction rate, enabling the development of more accurate particle-based simulations without sacrificing the convenience afforded by an analytic expression.

## II. THE EVOLUTION OF THE CLOSEST MOLECULE

To model the trimolecular reaction in Eq. (1.5) we consider a domain  $\Omega$  of volume  $V$ , where  $V$  is finite but very large, that contains the three distinct chemical species, A, B and C, whose molecules are all initially well mixed (distributed uniformly at random) within  $\Omega$ . It is convenient to assume that the system contains a single molecule of A and B, and  $N_C = cV$  molecules of C where  $c$  is a well-mixed concentration of C molecules. In essence, we are assuming that distinct pairs of A and B molecules can be treated independently, which, just as in the bimolecular case, is a good approximation so long as molecules only interact on small spatial scales. Furthermore, we assume that the molecules diffuse independently within the volume. Under these assumptions, the system contains  $N_C$  distinct states, where each state contains the single molecule of A, the single molecule of B, and a particular C molecule.

To understand the dynamics of this system, it is instructive to initially restrict our attention to a single of the  $N_C$  distinct states. We will use  $D_i$  and  $\mathbf{x}_i$ , where  $i = 0, 1, 2$ , to denote the diffusion constant and the three-dimensional position of the molecules of A, B, and C, respectively. Since we are primarily concerned with the molecules' relative proximity it is convenient to transform the coordinate system into diffusive Jacobi coordinates or separation coordinates,

$$\eta_0 = \bar{\mathbf{x}}_2 \quad \text{and} \quad (2.1a)$$

$$\eta_i = \mathbf{x}_i - \bar{\mathbf{x}}_{i-1}, \quad i = 1, 2, \quad \text{where} \quad (2.1b)$$

$$\bar{\mathbf{x}}_i = \frac{\sum_{j=0}^i \mathbf{x}_j D_j^{-1}}{\sum_{k=0}^i D_k^{-1}}, \quad (2.1c)$$

is the *center of diffusion* of the first  $i + 1$  molecules and is analogous to the center of mass except that the positions are weighted by their inverse diffusion coefficients rather than their masses. These weights are chosen so that, under the coordinate transformation from  $\mathbf{x}_i$  to  $\eta_i$ , the Laplacian term in the diffusion equation remains diagonal, with no mixed derivative terms. That is, each vector  $\eta_i$  diffuses independently. This property is explored in greater detail by Flegg [51].

Since  $\eta_0$  is the center of diffusion of the three molecules, changes in it correspond to translations of the state within the domain. That is, varying  $\eta_0$  does not change the relative proximity of the molecules in the current state, so we will only consider initial and boundary conditions that are independent of  $\eta_0$ . As a result, the joint probability density to find the unreacted state is also independent of  $\eta_0$  and we will be concerned exclusively with  $\eta_1$  and  $\eta_2$ . As shown in Fig. 2,



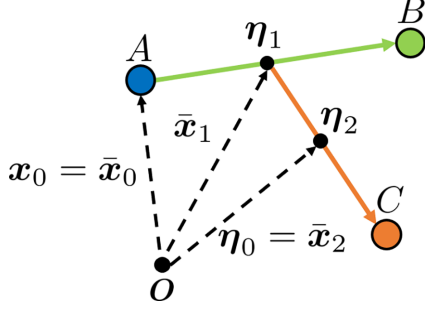


FIG. 2. The diffusive Jacobi coordinates for a system containing three molecules. The coordinate  $\eta_1$  describes the separation between the first two molecules, labeled A and B, while  $\eta_2$  describes the separation of the third molecule C from the center of diffusion of A and B which we denote  $\bar{x}_1$  and is defined in Eq. (2.1c). Finally,  $\eta_0$  is the center of diffusion of the three molecules ( $\bar{x}_2$ ) and changes in this coordinate correspond to translations of the state.

$\eta_1$  describes the separation between A and B as by definition  $\bar{x}_0 = x_0$ , and  $\eta_2$  describes the separation between C and the center of diffusion,  $\bar{x}_1$ , of A and B. In addition,  $\eta_1$  and  $\eta_2$  undergo independent linear diffusion with diffusion constants

$$\hat{D}_1 = D_1 + \bar{D}_0 \quad \text{and} \quad \hat{D}_2 = D_2 + \bar{D}_1, \quad (2.2)$$

respectively, where  $\bar{D}_j$  is the diffusion constant associated with  $\bar{x}_j$

$$\bar{D}_j = \frac{1}{\sum_{i=0}^j D_i^{-1}}. \quad (2.3)$$

The joint probability density,  $P(\eta, t)$ , to find the molecules in an unreacted state at time  $t$  is given by the diffusion equation

$$\frac{\partial P(\eta, t)}{\partial t} = \left[ \sum_{i=1}^2 \hat{D}_i \hat{\nabla}_i^2 \right] P(\eta, t), \quad (2.4)$$

where  $\eta = \{\eta_1, \eta_2\}$  is the state vector for the system and  $\hat{\nabla}_i^2$  denotes the Laplacian with respect to the coordinates of  $\eta_i$ . Since the system contains only a single molecule of A and B, the entire system is absorbed when a reaction occurs. For the trimolecular reaction in Eq. (1.5) a general proximity-based reaction condition can be defined as the absorbing boundary,

$$\partial\Omega_R = \{(\eta_1, \eta_2) : r_1 = f(r_2)\}, \quad (2.5)$$

where  $0 \leq f(r_2) \leq \sigma_{\max}$  is a monotonically decreasing function of  $r_2$  (recall that  $r_i = \|\eta_i\|$ ) and  $\sigma_{\max}$  is a small positive constant relative to the support of  $f$ . Furthermore, we assume that  $\sigma_{\max}$  is small enough that:

(1) The reaction is diffusion-limited, which requires the timescale for molecules of A and B to come into contact, characterized by  $V/(\hat{D}_1\sigma_{\max})$ , to be much longer than the timescale on which they react once in contact.

(2) Pairs of A and B molecules can be considered independently, which requires that  $\sigma_{\max}^3 a \ll 1$  and  $\sigma_{\max}^3 b \ll 1$ , where  $a$  and  $b$  denote the respective reactant concentrations.

(3) For  $r_2$  of  $O(1)$  or greater, we have  $\hat{D}_2\sigma_{\max}^2/(\hat{D}_1r_2^2) \ll 1$ , which we require for the forthcoming singular perturbation analysis to be valid.

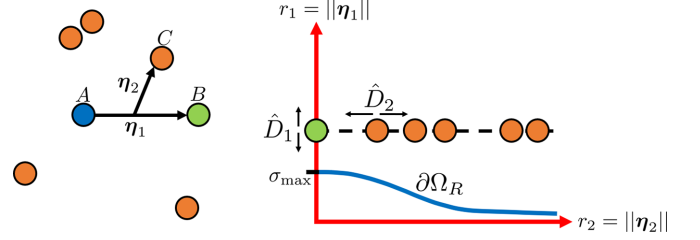


FIG. 3. The state space for a system that contains a single molecule of A (the blue point), a single molecule of B (the green point), and five molecules of C (the orange points). Each combination of A and B with a particular molecule of C gives a point within the state space on the right, shown by the orange points. The position of the B molecule relative to the A molecule defines a manifold of constant  $\eta_1$  that all states lie on. This manifold diffuses in  $\eta_1$  in accordance with Eq. (2.7a) and the states on the manifold diffuse independently in  $\eta_2$  according to Eq. (2.7b). The reaction boundary  $\partial\Omega_R$ , defined in Eq. (2.5), is shown as the blue curve and attains a maximum value of  $\sigma_{\max}$  at  $r_2 = 0$ . The first state to cross  $\partial\Omega_R$  will be absorbed.

According to this reaction boundary, the distance at which the molecules of A and B react is mediated by their relative proximity to the molecule of C rather than being fixed as it is in the bimolecular case. Moreover, the monotonic decay of the reaction boundary reflects the physical notion that reactions become more likely as the relative proximity between the three molecules reduces. In the case where the system contains a single molecule of C its evolution is governed by Eq. (2.4) subject to the inner boundary condition

$$P(\eta \in \partial\Omega_R, t) = 0. \quad (2.6)$$

However, in general this particular state will not be the first to cross  $\partial\Omega_R$  and so to model the full system, we must consider  $N_C$  distinct states; one for each combination of A, B, and a particular C molecule as shown in Fig. 3.

For any single particular state,  $\eta_1$  and  $\eta_2$  diffuse independently, so that the joint probability density can be written as,  $P(\eta, t) = P_1(\eta_1, t)P_2(\eta_2, t)$ , where the probability densities  $P_1$  and  $P_2$  evolve according to

$$\left[ \frac{\partial}{\partial t} - \hat{D}_1 \hat{\nabla}_1^2 \right] P_1(\eta_1, t) \equiv \mathcal{L}_1 P_1(\eta_1, t) = 0 \quad \text{and} \quad (2.7a)$$

$$\left[ \frac{\partial}{\partial t} - \hat{D}_2 \hat{\nabla}_2^2 \right] P_2(\eta_2, t) \equiv \mathcal{L}_2 P_2(\eta_2, t) = 0. \quad (2.7b)$$

Here  $\mathcal{L}_1$  and  $\mathcal{L}_2$  are diffusion operators on the three-dimensional spaces defined by  $\eta_1$  and  $\eta_2$ , respectively. Since every state shares the same molecule of B, all states lie on manifolds of constant  $\eta_1$  and the specific instance of  $\eta_1$  diffuses according to Eq. (2.7a). On this manifold, states diffuse independently in the three-dimensional space defined by  $\eta_2$  in accordance with Eq. (2.7b). The first state incident on the inner boundary  $\partial\Omega_R$  will cause the entire system to be absorbed, and since  $f$  is monotonic, this state will be the one with the minimum  $r_2$ . That is, we wish to know the dynamics of the state that contains the molecule of C that is closest to the center of diffusion of A and B.

If the system is well mixed, then we can assume that the  $\eta_2$  coordinates of the  $N_C$  states are uniformly and independently

distributed throughout  $\Omega$ . Now consider a particular molecule of C and let  $\mathbf{Z}_2$  denote the event that this particular molecule is associated with the minimum  $r_2$  when compared with any other C molecule in the system. Since the molecules are well mixed, the probability that an arbitrary C molecule has the minimum  $r_2$  at time  $t$  is

$$\Pr(\mathbf{Z}_2, t) = \frac{1}{N_C}. \quad (2.8)$$

The probability that a particular molecule of C has the minimum  $r_2$  at time  $t$  given it has a known  $\eta_2$ , is equal to the probability that all the other  $N_C - 1$  molecules of C lie outside a spherical region  $V_2$ , of radius  $r_2$  that is centered on the origin. That is,

$$\Pr(\mathbf{Z}_2, t|\eta_2) = \left[1 - \int_{V_2} P_2(\eta'_2, t) dV'_2\right]^{N_C-1}, \quad (2.9)$$

where  $dV'_2$  is an elemental volume for the coordinates of  $\eta'_2$ . The probability density,  $P(\eta_2, t|\mathbf{Z}_2)$ , for finding a particular molecule of C at  $\eta_2$  at time  $t$ , given that it has the smallest  $r_2$  of any molecule of C in the system, can be found by using Bayes's theorem in combination with Eqs. (2.8) and (2.9),

$$P(\eta_2, t|\mathbf{Z}_2) = N_C P_2(\eta_2, t) \left[1 - \int_{V_2} P_2(\eta'_2, t) dV'_2\right]^{N_C-1}. \quad (2.10)$$

The system is very large and, in the limit that  $V$ —and hence  $N_C$ —tends to infinity,  $P\mathbf{Z}_2, t$  goes to zero in accordance with Eq. (2.8). To ensure we take the appropriate limit in Eq. (2.10) we define the scaled probability densities

$$\Phi(\eta_2, t) = \frac{P(\eta_2, t|\mathbf{Z}_2)}{c} \quad \text{and} \quad (2.11a)$$

$$\varphi(\eta_2, t) = \frac{N_C P_2(\eta_2, t)}{c}, \quad (2.11b)$$

which when substituted into Eq. (2.10) give

$$\Phi(\eta_2, t) = \varphi(\eta_2, t) \left[1 - \frac{c}{N_C} \int_{V_2} \varphi(\eta'_2, t) dV'_2\right]^{N_C-1}. \quad (2.12)$$

Taking the limit  $N_C \rightarrow \infty$  in Eq. (2.12) gives

$$\Phi(\eta_2, t) = \varphi(\eta_2, t) \exp\left(-c \int_{V_2} \varphi(\eta'_2, t) dV'_2\right), \quad (2.13)$$

and then using Eq. (2.7b), we find that  $\Phi(\eta_2, t)$  evolves according the advection-diffusion equation

$$\begin{aligned} \frac{\partial \Phi(\eta_2, t)}{\partial t} &= \hat{D}_2 \hat{\nabla}_2^2 \Phi(\eta_2, t) + \hat{D}_2 \hat{\nabla}_2 \\ &\quad \cdot (4\pi r_2^2 c \varphi(\eta_2, t) \Phi(\eta_2, t) \hat{\mathbf{r}}_2), \end{aligned} \quad (2.14)$$

where  $\hat{\mathbf{r}}_2$  is the unit outward facing normal vector of a sphere of radius  $r_2$  centered on the origin. A derivation of this result can be found in Appendix A.

Equation (2.14) can be written entirely in terms of  $\Phi(\eta_2, t)$  by noting that  $P(\mathbf{Z}_2, t|\eta_2)$  is also equal to the probability that the closest molecule is not inside the spherical region  $V_2$ . That

is, in addition to Eq. (2.9) we must also have

$$\begin{aligned} \Pr(\mathbf{Z}_2, t|\eta_2) &= 1 - \int_{V_2} P(\eta'_2, t|\mathbf{Z}_2) dV'_2 \\ &= \int_{r_2}^{\infty} P(\eta'_2, t|\mathbf{Z}_2) 4\pi r_2'^2 dr_2', \end{aligned} \quad (2.15)$$

Bayes's theorem then gives

$$P_2(\eta_2, t) = \frac{P(\eta_2, t|\mathbf{Z}_2) \Pr(\mathbf{Z}_2, t)}{\Pr(\mathbf{Z}_2, t|\eta_2)}, \quad (2.16)$$

from which we conclude

$$c\varphi(\eta_2, t) = \frac{\Phi(\eta_2, t)}{\int_{r_2}^{\infty} \Phi(\eta'_2, t) 4\pi r_2'^2 dr_2'}. \quad (2.17)$$

Substituting Eq. (2.17) into Eq. (2.14), and then using Eq. (2.11a), we arrive at the governing equation for  $P(\eta_2, t|\mathbf{Z}_2)$ ,

$$\begin{aligned} \frac{\partial P(\eta_2, t|\mathbf{Z}_2)}{\partial t} &= \hat{D}_2 \hat{\nabla}_2^2 P(\eta_2, t|\mathbf{Z}_2) + \hat{D}_2 \hat{\nabla}_2 \\ &\quad \cdot \left( \frac{r_2^2 (P(\eta_2, t|\mathbf{Z}_2))^2 \hat{\mathbf{r}}_2}{\int_{r_2}^{\infty} P(\eta'_2, t|\mathbf{Z}_2) r_2'^2 dr_2'} \right). \end{aligned} \quad (2.18)$$

Finally, we note that since  $\eta_1$  diffuses independently of  $\eta_2$ , the evolution of the joint probability density  $P(\eta, t|\mathbf{Z}_2)$  for finding the separation of the state with the minimum value of  $r_2$  is governed by

$$\begin{aligned} \frac{\partial P(\eta, t|\mathbf{Z}_2)}{\partial t} &= \left[ \sum_{i=1}^2 \hat{D}_i \hat{\nabla}_i^2 \right] P(\eta, t|\mathbf{Z}_2) + \hat{D}_2 \hat{\nabla}_2 \\ &\quad \cdot \left( \frac{r_2^2 (P(\eta, t|\mathbf{Z}_2))^2 \hat{\mathbf{r}}_2}{\int_{r_2}^{\infty} P(\eta_1, \eta'_2, t|\mathbf{Z}_2) r_2'^2 dr_2'} \right). \end{aligned} \quad (2.19)$$

The linear diffusion terms in Eq. (2.19) describe the independent Brownian motion of  $\eta_1$  and  $\eta_2$ , while the advection towards  $\eta_2 = \mathbf{0}$  represents the flux of the likelihood that the C molecule with the second-smallest  $\|\eta_2\|$  value diffuses over the sphere of radius  $r_2$  set by the currently closest C molecule. In other words, it accounts for the fact that the molecule of C that is the second-closest to the origin can diffuse inwards and become the closest molecule to the origin.

In the bimolecular case considered by Smoluchowski, the probability density relates to the likelihood of finding any molecule of B at a particular position, while in the trimolecular case we have been careful to restrict our attention to the state associated with the closest molecule of C. This disparity arises because we have assumed that our trimolecular reaction boundary  $\partial\Omega_R$  extends a very small distance, at most  $\sigma_{\max}$ , in the  $\eta_1$  direction, but may be comparatively long in the  $\eta_2$  direction. In the extreme case where  $f(r_2) = \sigma_{\max}$  any molecule of C will satisfy the reaction condition regardless of its proximity to A and B once  $r_1 = \sigma_{\max}$ , and we must specify a particular molecule of C to be involved in the reaction to avoid ambiguity. Moreover, particle-based simulations of reaction-diffusion systems often update the position of molecules using finite time steps [64–66] which means that molecules are moved using small discrete displacements rather than continuously. If a pair of A and B molecules is such that their separation  $r_1$  is just larger than  $f(r_2)$ , then

they can ‘jump’ through the reaction boundary during the next time step, so that  $r_1 < f(r_2)$  following the position updates. At this point, there can again be multiple molecules of C close enough to satisfy the reaction condition, even if  $f$  is not constant. In theory, the same problem exists when simulating bimolecular reactions and the distribution for the closest molecule to Smoluchowski’s reaction boundary can be derived analytically [52]. However, in practice  $\sigma$  is small enough that the likelihood that two molecules of B are close enough to A to react at any given moment is insignificant. Thus, unlike the trimolecular case, it is always clear which molecule of B should react with a particular molecule of A.

To determine a unique solution for  $P(\eta, t|Z_2)$  we require appropriate initial and boundary conditions. To this end we assume that initially all the molecules are distributed uniformly at random throughout  $\Omega$  so that the initial condition is given by the boundary-free steady-state solution of Eq. (2.19),

$$P(\eta, 0|Z_2) = \frac{c}{V} \exp\left(\frac{-4\pi cr_2^3}{3}\right). \quad (2.20)$$

Moreover, we know that the system will be absorbed when the state associated with the closest molecule of C crosses  $\partial\Omega_R$ , which leads to the inner boundary condition

$$P(\eta \in \partial\Omega_R, t|Z_2) = 0. \quad (2.21)$$

Notice that this condition reduces to Eq. (2.6) when the domain contains only a single molecule of C. Infinitely far from  $\partial\Omega_R$  in both the  $\eta_1$  and  $\eta_2$  direction, the probability density is unperturbed by the absorption of states on  $\partial\Omega_R$  so that

$$\lim_{r_1 \rightarrow \infty} P(\eta, t|Z_2) = \frac{c}{V} \exp\left(\frac{-4\pi cr_2^3}{3}\right) \quad \text{and} \quad (2.22a)$$

$$\lim_{r_2 \rightarrow \infty} P(\eta, t|Z_2) = \lim_{r_2 \rightarrow \infty} \frac{c}{V} \exp\left(\frac{-4\pi cr_2^3}{3}\right) = 0. \quad (2.22b)$$

Finally, the flux of the probability density in the  $\eta_2$  direction should vanish at  $r_2 = 0$  which amounts to requiring that

$$\frac{\partial P(\eta, t|Z_2)}{\partial r_2} = 0 \quad \text{at } r_2 = 0. \quad (2.23)$$

Equation (2.19), subject to the conditions in Eqs. (2.20)–(2.23), describes the evolution of the state that will cause the system to be absorbed. However, solving this PDE when  $\partial\Omega_R$  is chosen arbitrarily is very difficult. If  $\partial\Omega_R$  extends a small distance in both  $r_1$  and  $r_2$  [rather than just in  $r_1$  as assumed in Eq. (2.5)], then the advection term in Eq. (2.19) becomes negligible, and the problem reduces to the trimolecular generalization of Smoluchowski’s reaction condition considered by Flegg [51], for which an exact solution can be found. Outside of this regime, we are not aware of an exact solution, but it is possible to construct a leading-order solution using singular perturbation methods.

Similar to the bimolecular case considered by Smoluchowski, the full time-dependent solution of Eq. (2.19) will rapidly converge to a steady state, since  $\partial\Omega_R$  only extends a small distance in the  $\eta_1$  direction [47]. Thus, we will focus on computing the steady-state solution of the PDE, which will be radially symmetric in both  $\eta_1$  and  $\eta_2$  because the boundary conditions [Eqs. (2.20)–(2.23)] only depend on the

corresponding radial coordinates  $r_1$  and  $r_2$ . That is, the steady-state solution of Eq. (2.19), which we will denote  $P(r_1, r_2)$  henceforth, will only depend on  $r_1$  and  $r_2$ .

In the limit that  $\sigma_{\max} \rightarrow 0$ ,  $\partial\Omega_R$  becomes a sphere of radius 0 and, in effect, the absorbing boundary vanishes. In this case, the steady-state solution to Eq. (2.19) is the initial condition from Eq. (2.20). However, this solution has no  $r_1$  dependence and so will never satisfy the boundary condition on  $\partial\Omega_R$  for any finite value of  $\sigma_{\max}$ . This behavior indicates that there exists a boundary layer [67] near  $\partial\Omega_R$ . That is, in the vicinity of the inner boundary, we expect the steady-state solution to change rapidly from the boundary-free steady-state solution to one that satisfies the boundary condition.

In Appendix B we perform a perturbation expansion of  $P(r_1, r_2)$  near  $\partial\Omega_R$  and apply standard singular perturbation techniques to derive the leading-order term

$$P_0(r_1, r_2) = \frac{c}{V} \exp\left(\frac{-4\pi cr_2^3}{3}\right) \left(1 - \frac{f(r_2)}{r_1}\right), \quad (2.24)$$

which serves as the leading-order approximation to  $P$  in that it neglects corrections of  $O(\sigma_{\max}^2)$ . We henceforth refer to  $P_0$  as the leading-order solution.

The leading-order solution can be used to approximate the steady-state reaction rate, which is the total flux of  $P(r_1, r_2)$  over  $\partial\Omega_R$ . The outward facing unit normal vector to  $\partial\Omega_R$  is

$$\hat{n}_{\text{out}} = -\left(1 + \left(\sigma_{\max} \frac{dF(r_2)}{dr_2}\right)^2\right)^{-\frac{1}{2}} \left(\hat{r}_1 - \sigma_{\max} \frac{dF(r_2)}{dr_2} \hat{r}_2\right), \quad (2.25)$$

therefore, to first order in  $\sigma_{\max}$ , only the diffusive flux in the  $\hat{r}_1$  direction contributes. That is, the steady-state reaction rate can be approximated by

$$K_1(c) = \int_0^\infty \left(\hat{D}_1 \frac{\partial P(r_1, r_2)}{\partial r_1} \hat{r}_1 \cdot 4\pi (f(r_2))^2 \hat{r}_1\right) 4\pi r_2^2 dr_2, \quad (2.26)$$

which can be simplified to

$$K_1(c) = \int_0^\infty \frac{4\pi \hat{D}_1 f(r_2)}{V} c \exp\left(\frac{-4\pi cr_2^3}{3}\right) 4\pi r_2^2 dr_2, \quad (2.27)$$

using Eq. (2.24) and neglecting the  $O(\sigma_{\max}^2)$  terms.

Equation (2.27) matches the expression used by Kearney and Flegg [50] to determine the function  $f(r_2)$ , which defines the boundary  $\partial\Omega_R$  required to reproduce a given reaction rate  $K_1(c)$ . However, to arrive at this expression, several contributions to the flux across  $\partial\Omega_R$  must be ignored. First, there is an  $O(\sigma_{\max}^2)$  correction to the leading-order solution and hence to the diffusive flux in the  $\hat{r}_1$  direction. In addition, there is an  $O(\sigma_{\max}^2)$  contribution to the flux that arises from the diffusive and advective fluxes in the  $\hat{r}_2$  direction. Neglecting these contributions means that the functional form derived for  $\partial\Omega_R$  will not be exact, resulting in small errors in the reaction rate reproduced by particle-based simulations that use this reaction boundary. Although these errors were known to Kearney and Flegg [50], they did not examine them in detail because it was difficult to isolate them from other sources of error present in their simulations.

Ideally, we would quantify these corrections analytically by continuing our singular perturbation analysis. However, as shown in Appendix B, standard techniques are not sufficient to derive the  $O(\sigma_{\max}^2)$  term in the perturbation expansion of  $P(r_1, r_2)$ . Therefore, to quantify the expected  $O(\sigma_{\max}^2)$  corrections, we seek a finite-element solution to the problem that can be compared to the leading-order solution in Eq. (2.24).

### III. MIXED-PRIMAL FORMULATION

The quantity of primary concern for particle-based simulations is the steady-state reaction rate, which corresponds to the flux of  $P(r_1, r_2)$  over the reaction boundary  $\partial\Omega_R$ . One approach to compute this flux is to use a reconstruction from the finite-element solution to the original form of the PDE in Eq. (2.19) (see, e.g., Ref. [68]), but we opt for using a mixed-primal reformulation of the problem (which might be more appropriate to preserve the divergence structure [69]), and solve for the flux

$$s(r_1, r_2) = -\left(\nabla P(r_1, r_2) + \frac{r_2^2 P(r_1, r_2)^2}{Q(r_1, r_2)} \hat{\mathbf{r}}_2\right), \quad (3.1)$$

directly, where

$$\nabla P(r_1, r_2) = \frac{\partial P(r_1, r_2)}{\partial r_1} \hat{\mathbf{r}}_1 + \frac{\partial P(r_1, r_2)}{\partial r_2} \hat{\mathbf{r}}_2. \quad (3.2)$$

Notice that we have introduced the *density moment*,

$$Q(r_1, r_2) = \int_{r_2}^{\infty} P(r_1, r'_2) r_2'^2 dr'_2, \quad (3.3)$$

which enables us to avoid directly calculating the integral in the Eq. (2.19). The steady state is now governed by a coupled system of PDEs

$$s(r_1, r_2) + \left(\nabla P(r_1, r_2) + \frac{r_2^2 P(r_1, r_2)^2}{Q(r_1, r_2)} \hat{\mathbf{r}}_2\right) = 0, \quad (3.4a)$$

$$\nabla \cdot (Ds(r_1, r_2)) = 0, \quad \text{and} \quad (3.4b)$$

$$\frac{\partial Q(r_1, r_2)}{\partial r_2} + r_2^2 P(r_1, r_2) = 0, \quad (3.4c)$$

where  $D$  is a matrix of the diffusion coefficients such that,

$$D = \begin{bmatrix} \hat{D}_1 & 0 \\ 0 & \hat{D}_2 \end{bmatrix}, \quad (3.5)$$

and  $\nabla \cdot s(r_1, r_2)$  denotes the radial divergence of  $s(r_1, r_2)$ , that is,

$$\begin{aligned} \nabla \cdot s(r_1, r_2) &= \frac{1}{r_1^2} \frac{\partial}{\partial r_1} (r_1^2 s(r_1, r_2) \cdot \hat{\mathbf{r}}_1) \\ &+ \frac{1}{r_2^2} \frac{\partial}{\partial r_2} (r_2^2 s(r_1, r_2) \cdot \hat{\mathbf{r}}_2). \end{aligned} \quad (3.6)$$

The corresponding steady-state reaction rate can be computed straightforwardly by evaluating

$$K(c) = \int_0^{\infty} Ds(r_1, r_2) \cdot \hat{\mathbf{n}}_{\text{out}} (4\pi f(r_2) r_2)^2 dr_2, \quad (3.7)$$

where we recall that  $\hat{\mathbf{n}}_{\text{out}}$  is the outward facing unit normal vector to  $\partial\Omega_R$ .

In principle the boundary conditions for  $P(r_1, r_2)$  remain unchanged except that the no-flux condition defined in Eq. (2.23) now defines a boundary condition on  $s(r_1, r_2)$

$$s(r_1, r_2) \cdot \hat{\mathbf{r}}_2 = 0 \quad \text{at } r_2 = 0. \quad (3.8)$$

However, we have assumed that the domain  $\Omega$  is very large (effectively infinite) in defining these conditions, and representing such a large domain inherently limits the resolution of the finite-element mesh. This is problematic because we must be able to resolve the rapid change in the solution expected within the boundary layer near  $\partial\Omega_R$ . Therefore, it is necessary to consider a domain amenable for the finite-element discretization

$$\Omega_{\text{FE}} = \{(r_1, r_2) : f(r_2) \leq r_1 \leq r_1^{\max}, 0 \leq r_2 \leq r_2^{\max}\}, \quad (3.9)$$

that is not necessarily sufficiently large for these boundary conditions to be valid. The inner boundary condition from Eq. (2.20) transfers trivially to  $\Omega_{\text{FE}}$ ,

$$P(r_1, r_2) = 0 \quad \text{on } r_1 = f(r_2), \quad (3.10)$$

but the remaining conditions in Eqs. (2.22a) and (2.22b) require more careful consideration.

We expect the leading-order contribution to  $P(r_1, r_2)$  to decay exponentially as  $r_2$  increases. The rate of decay is expected to match that of the value on the boundary, given in Eq. (2.22b), and so the value imposed at  $r_2 = r_2^{\max}$  very quickly approaches zero. Therefore, the error that arises from imposing

$$P(r_1, r_2) = \frac{c}{V} \exp\left(\frac{-4\pi c r_2^3}{3}\right) \quad \text{at } r_2 = r_2^{\max}, \quad (3.11)$$

for finite  $r_2^{\max}$ , very quickly approaches zero as  $r_2^{\max}$  is increased. Adopting this condition implies that we must also have

$$Q(r_1, r_2) = \frac{1}{4\pi V} \exp\left(\frac{-4\pi c r_2^3}{3}\right) \quad \text{at } r_2 = r_2^{\max}. \quad (3.12)$$

In contrast, as  $r_1$  increases, we expect the leading-order solution to decay to the boundary condition in Eq. (2.22a) with the reciprocal of  $r_1$ . That is, we expect the solution to converge to the outer solution much more slowly in the  $\hat{\mathbf{r}}_1$  direction than in the  $\hat{\mathbf{r}}_2$  direction and require  $r_1^{\max}$  to be significantly larger than  $r_2^{\max}$  for the boundary condition to be correct. Even if  $r_1^{\max}$  is  $O(1/\sigma_{\max})$  adopting the boundary condition in Eq. (2.22a) incurs an  $O(\sigma_{\max}^2)$  error that arises from the  $O(\sigma_{\max})$  contribution to  $P(r_1, r_2)$ . To avoid introducing this unnecessary error we use the leading-order solution to modify the boundary condition for finite  $r_1^{\max}$  and instead impose

$$P(r_1, r_2) = \frac{c}{V} \exp\left(\frac{-4\pi c r_2^3}{3}\right) \left(1 - \frac{f(r_2)}{r_1}\right) \quad \text{at } r_1 = r_1^{\max}. \quad (3.13)$$

This boundary condition neglects any  $O(\sigma_{\max}^2)$  corrections to the solution; however, we expect these corrections to decay polynomially with increasing  $r_1$  similar to the  $O(\sigma_{\max})$  term in the leading-order solution. Therefore, the error introduced by adopting this condition can be made negligible by making  $r_1^{\max}$  sufficiently large.



The finite-element formulation of Eq. (3.4) along with convergence testing for the adopted scheme is provided in Appendix C.

#### IV. RESULTS

To examine the accuracy of the leading-order solution in Eq. (2.24) in this section we compare it to the finite-element solution of Eq. (3.4), which is the mixed-primal reformulation of the steady-state version of the original PDE in Eq. (2.19). For this comparison the reaction boundary is

$$\partial\Omega_R = \left\{ (\eta_1, \eta_2) : r_1 = \sigma_{\max} \exp\left(\frac{-4\pi\Gamma r_2^3}{3}\right) \right\}, \quad (4.1)$$

where  $\Gamma > 0$  is a parameter that controls the rate at which the height of the boundary decays as  $r_2$  increases, and the finite-element solution is computed over the domain

$$\Omega_{\text{FE}} = \left\{ (r_1, r_2) : \sigma_{\max} \exp\left(\frac{-4\pi\Gamma r_2^3}{3}\right) \leq r_1 \leq 5, 0 \leq r_2 \leq 5 \right\}. \quad (4.2)$$

Using Eq. (2.27) we find that the steady-state reaction rate for this domain can be approximated by

$$K_1(c) = \frac{4\pi\hat{D}_1\sigma_{\max}c}{V_{\text{FE}}(c + \Gamma)}, \quad (4.3)$$

where  $V_{\text{FE}} = (4/3)\pi(r_1^{\max})^3$  and we have implicitly adopted the limit  $r_2^{\max} \rightarrow \infty$  which introduces a negligible error compared to integrating up until  $r_2^{\max} = 5$ . In Sec. IV A we examine the steady-state finite-element solution for this particular choice of  $\partial\Omega_R$  and compare the corresponding reaction rate with Eq. (4.3). Then in Sec. IV B we demonstrate how to alter  $\partial\Omega_R$  so that the observed reaction rate better replicates the desired reaction rate. In other words, we show how to correct for the errors incurred when adopting the approximation in Eq. (4.3).

The reaction boundary defined in Eq. (4.1) is of particular interest because it was used by Kearney and Flegg [50] in their particle-based simulation of the system we are considering. Although Kearney and Flegg briefly compared the reaction rate obtained from their simulation to  $K_1(c)$ , their results contained additional sources of error beyond those introduced by the approximation itself, making it impossible to isolate these contributions. In contrast, the finite-element solution presented here is free from such confounding factors, making it possible to isolate the higher-order corrections to steady-state reaction rate.

Before proceeding we note that all quantities in this article are assumed to be dimensionless. Lengths are nondimensionalized with respect to a characteristic length scale, chosen such that the length of the domain is  $r_1^{\max} = r_2^{\max} = 5$ . Therefore, any concentrations stated denote the number of particles per unit of dimensionless volume  $V_{\text{FE}}$ . Unless otherwise stated all molecules are assumed to diffuse at equal dimensional rates, and a characteristic timescale is chosen such that the dimensionless diffusion coefficients of species A, B, and C are all equal to 1. The corresponding dimensionless diffusion coefficients for  $\eta_1$  and  $\eta_2$  are  $\hat{D}_1 = 2$  and  $\hat{D}_2 = 1.5$ , respectively.

#### A. Comparison of finite-element and leading-order solutions

To isolate the  $O(\sigma_{\max}^2)$  corrections to the leading-order solution  $P_0$ , we consider the (scaled) difference  $\delta P(r_1, r_2)$  between the finite-element approximation of the density  $P(r_1, r_2)$ , which we denote by  $P_h(r_1, r_2)$ , and Eq. (2.24)

$$\delta P(r_1, r_2) = 4\pi r_2^2 \left( P_h(r_1, r_2) - \frac{c}{V_{\text{FE}}} \exp\left(\frac{-4\pi c r_2^3}{3}\right) \times \left( 1 - \frac{\sigma_{\max}}{r_1} \exp\left(\frac{-4\pi\Gamma r_2^3}{3}\right) \right) \right). \quad (4.4)$$

The factor of  $4\pi r_2^2$  is included since it is more convenient to work with the scaled probability density  $4\pi r_2^2 P(r_1, r_2)$ , which represents the probability to find the closest molecule of C on the surface of a sphere of radius  $r_2$  that is centered on the origin. Figure 4 depicts  $\delta P$  in the case that  $\sigma_{\max} = 0.1$  and  $\Gamma = 1$ , while we set  $c = 10$  because it results in a sufficiently concentrated density profile for the associated flux to be easily visible near  $\partial\Omega_R$ ; see Fig. 5. The surface plot in Fig. 4(a) displays the entirety of  $\Omega_{\text{FE}}$  while Fig. 4(b) displays a subdomain that only extends to  $r_1 = 0.5$  and  $r_2 = 1$ .

As expected, the solutions differ the most near  $\partial\Omega_R$  while the difference decays as both  $r_1$  and  $r_2$  increase. Notice that while  $\delta P$  decays very rapidly to zero as  $r_2$  increases, it decays much more slowly as  $r_1$  increases and remains finite even very close to the boundary at  $r_1 = r_1^{\max}$ ;  $\delta P$  vanishes on this boundary since we enforce equality between the solutions there. This suggests that, similarly to the  $O(\sigma_{\max})$  contribution present in Eq. (2.24), the  $O(\sigma_{\max}^2)$  contributions to the solution decay exponentially as  $r_2$  increases, but polynomially as  $r_1$  increases. Moreover, we can see that  $P_0$  underestimates the probability, resulting in the yellow region where  $\delta P(r_1, r_2) > 0$ , that the closest molecule is close to the origin and instead favors larger values of  $r_2$ , resulting in the dark blue region where  $\delta P(r_1, r_2) < 0$ . This is because the leading-order solution results from considering the limit  $\sigma_{\max}^2 \rightarrow 0$  in Eq. (B2), which amounts to ignoring both the diffusive motion in the  $\hat{r}_2$  direction and, more severely, the advective motion towards the origin in this direction.

Similarly, when approximating the steady-state reaction rate using  $K_1(c)$  from Eq. (2.27), we only consider the  $O(\sigma_{\max})$  contributions to the flux of the probability density over  $\partial\Omega_R$ . This effectively ignores the contribution to this reaction rate from the flux in the  $\hat{r}_2$  direction as well as an  $O(\sigma_{\max}^2)$  correction to the contribution in the  $\hat{r}_1$  direction, which arises from the correction of the same order to  $P_0$ . The (scaled)  $O(\sigma_{\max}^2)$  correction to the diffusive flux in the  $\hat{r}_1$  direction is calculated using the finite-element approximation to the full flux  $s(r_1, r_2)$ , which we denote by  $s_h(r_1, r_2)$ ,

$$\delta s_1(r_1, r_2) = 4\pi r_2^2 \hat{D}_1 (s_h(r_1, r_2) \cdot \hat{r}_1 + \nabla P_0(r_1, r_2) \cdot \hat{r}_1), \quad (4.5)$$

and is shown in Fig. 5(a), where in this case

$$\nabla P_0(r_1, r_2) \cdot \hat{r}_1 = \frac{c\sigma_{\max}}{V_{\text{FE}}r_1^2} \exp\left(\frac{-4\pi(c + \Gamma)r_2^3}{3}\right). \quad (4.6)$$

Since  $K_1(c)$  ignores the flux in the  $\hat{r}_2$  direction entirely, the (scaled)  $O(\sigma_{\max}^2)$  correction to this component is simply the

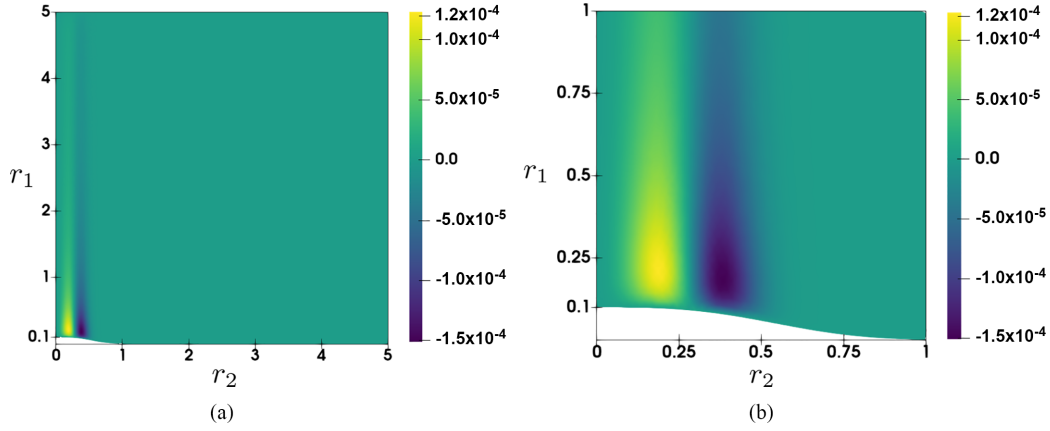


FIG. 4. The (scaled) difference  $\delta P(r_1, r_2)$ , defined in Eq. (4.4), between the steady-state finite-element solution  $P_h(r_1, r_2)$  and the leading-order solution  $P_0(r_1, r_2)$  for  $\hat{D}_1 = 2$ ,  $\hat{D}_2 = 1.5$ ,  $\sigma_{\max} = 0.1$ ,  $\Gamma = 1$ , and  $c = 10$ . The leading-order solution underestimates the probability, resulting in the yellow region where  $\delta P(r_1, r_2) > 0$ , that the closest molecule of C is near to the origin and instead favors larger values of  $r_2$ , which results in the dark blue region where  $\delta P(r_1, r_2) < 0$ . This discrepancy arises because  $P_0$  neglects the advection towards the origin in the  $\hat{r}_2$  (horizontal) direction. The difference appears most pronounced near the bottom boundary  $\partial\Omega_R$ , defined in Eq. (4.1), but this is because the solutions decay with increasing  $r_1$ . The surface plot in (a) shows the finite-element domain from Eq. (4.2), while the plot in (b) shows the subdomain  $\{(r_1, r_2) : \sigma_{\max} \exp(\frac{-4\pi\Gamma r_2^3}{3}) \leq r_1 \leq 1, 0 \leq r_2 \leq 1\}$ .

total flux in this direction

$$\delta s_2(r_1, r_2) = 4\pi r_2^2 \hat{D}_2 s_h(r_1, r_2) \cdot \hat{r}_2, \quad (4.7)$$

and is shown in Fig. 5(b). In each case, we have restricted our attention to a subdomain of  $\Omega_{\text{FE}}$  that only extends to  $r_1 = 0.5$  and  $r_2 = 1$ , since the flux is negligible outside this subdomain. The behavior of  $\delta s_1$  mimics that of  $\delta P$  in that the flux of the leading-order solution underestimates the magnitude of the diffusive flux in the  $\hat{r}_1$  direction for small values of  $r_2$ , resulting in the dark blue region where  $\delta s_1(r_1, r_2) < 0$ , while overestimating it at larger values, resulting in the yellow region where  $\delta s_1(r_1, r_2) > 0$ . In addition, we can see that there will also be a correction in the same vicinity due to  $\delta s_2$ . Notice that both components of the flux point in the opposite direction to the respective radial unit vectors  $\hat{r}_1$  and  $\hat{r}_2$ .

To better contextualize these corrections we now consider the total flux of  $P_h$  over  $\partial\Omega_R$ ,

$$K_{\text{FE}}(c) = \int_0^{r_2^{\max}} D s_h(r_1, r_2) \cdot \hat{n}_{\text{out}} (4\pi f(r_2) r_2)^2 dr_2, \quad (4.8)$$

which serves as a proxy for the exact reaction rate  $K(c)$ , although we will continue to use the subscript “FE” to distinguish this approximate rate. We are concerned with how the corrections to the flux shown in Fig. 5 affect this rate, and to quantify these contributions, we define three relative errors,

$$\delta K(c) = \frac{K_{\text{FE}}(c) - K_1(c)}{K_1(c)}, \quad (4.9a)$$

$$\delta K^1(c) = \frac{1}{K_1(c)} \left( \int_0^{r_2^{\max}} D s_h(r_1, r_2) \cdot \hat{n}_1 (4\pi f(r_2) r_2)^2 dr_2 - K_1(c) \right), \quad (4.9b)$$

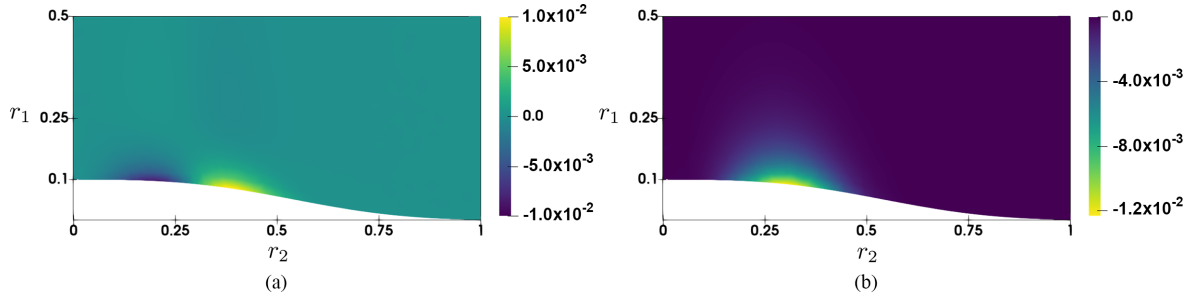


FIG. 5. The corrections to the flux of the probability density that are neglected by the approximation  $K_1(c)$  to the steady-state reaction rate defined in Eq. (2.27), for  $\hat{D}_1 = 2$ ,  $\hat{D}_2 = 1.5$ ,  $\sigma_{\max} = 0.1$ ,  $\Gamma = 1$ , and  $c = 10$ . The surface plot in (a) shows the (scaled) correction  $\delta s_1(r_1, r_2)$  to the diffusive flux in the  $\hat{r}_1$  (vertical) direction defined by Eq. (4.5). The diffusive flux of the leading-order solution  $P_0(r_1, r_2)$  underestimates the magnitude of the  $\hat{r}_1$  component of the finite-element solution  $s_h(r_1, r_2)$  for values of  $r_2$  less than approximately 0.25, resulting in the dark blue region where  $\delta s_1(r_1, r_2) < 0$ . In contrast, the magnitude of this flux is overestimated for larger values of  $r_2$ , resulting in the yellow region where  $\delta s_1(r_1, r_2) > 0$ . Similarly, the surface plot in (b) shows the (scaled) correction  $\delta s_2(r_1, r_2)$  to the flux accounted for by  $K_1(c)$  in the  $\hat{r}_2$  (horizontal) direction defined by Eq. (4.7). Since  $K_1(c)$  entirely neglects the flux in this direction over  $\partial\Omega_R$ , as it is an  $O(\sigma_{\max}^2)$  contribution, this correction is simply the  $\hat{r}_2$  component of the finite-element solution  $s_h(r_1, r_2)$ . Both plots display the subdomain  $\{(r_1, r_2) : 0 \leq r_1 \leq 0.5, 0 \leq r_2 \leq 1\}$ .

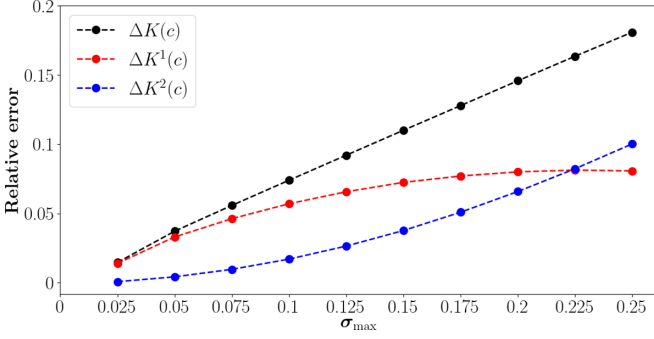


FIG. 6. The relative error between the steady-state reaction rate  $K_{\text{FE}}(c)$  from Eq. (4.8), and the approximate reaction rate  $K_1(c)$ , given by Eq. (2.27), calculated for  $c = 1$ ,  $\hat{D}_1 = 2$ ,  $\hat{D}_2 = 1.5$ ,  $\Gamma = 1$ , while  $\sigma_{\text{max}}$  is increased from 0.025 to 0.25 in intervals of 0.025. The steady-state reaction rate is defined as the total flux of the probability density over the boundary  $\partial\Omega_R$ , defined by Eq. (4.1). The black line shows the total relative error  $\delta K(c)$ , defined in Eq. (4.9a), between  $K_{\text{FE}}(c)$  and  $K_1(c)$ . This error arises because  $K_1(c)$  neglects  $O(\sigma_{\text{max}}^2)$  contributions to the flux over  $\partial\Omega_R$ . Since there are contributions of this order over  $\partial\Omega_R$  in both the  $\hat{r}_1$  and  $\hat{r}_2$  directions, we quantify them separately using the relative errors  $\delta K^1(c)$  and  $\delta K^2(c)$ , defined in Eqs. (4.9b) and (4.9c), and shown by the red, and blue lines respectively. That is,  $\delta K^1(c)$  and  $\delta K^2(c)$  represent the relative error that arises from ignoring  $O(\sigma_{\text{max}}^2)$  contributions to the flux over  $\partial\Omega_R$  in the  $\hat{r}_1$  and  $\hat{r}_2$  directions respectively. The finite-element solution used to calculate  $K_{\text{FE}}(c)$  was evaluated over the domain  $\Omega_{\text{FE}} = \{(r_1, r_2) : \sigma_{\text{max}} \exp(\frac{-4\pi\Gamma r_2^2}{3}) \leq r_1 \leq 5, 0 \leq r_2 \leq 5\}$ .

and

$$\delta K^2(c) = \frac{1}{K_1(c)} \int_0^{r_2^{\text{max}}} Ds_h(r_1, r_2) \cdot \hat{n}_2 (4\pi f(r_2) r_2)^2 dr_2, \quad (4.9c)$$

where  $\hat{n}_i = (\hat{n}_{\text{out}} \cdot \hat{r}_i) \hat{r}_i$ . Since  $K_1(c)$  only considers the diffusive flux of  $P_0$  over  $\partial\Omega_R$  in the  $\hat{r}_1$  direction,  $\delta K^1(c)$  essentially measures the relative error in the reaction rate that arises from neglecting  $O(\sigma_{\text{max}}^2)$  corrections to the flux of  $P$  in this direction. Similarly,  $\delta K^2(c)$  measures the relative error that arises from neglecting the diffusive and advective flux of  $P$  over  $\partial\Omega_R$  in the  $\hat{r}_2$  direction.

To explore how these errors behave as the shape of  $\partial\Omega_R$  changes, we fix  $c = 1$ ,  $\hat{D}_1 = 2$ ,  $\hat{D}_2 = 1.5$  and conduct two tests. In the first, we hold  $\sigma_{\text{max}} = 0.1$  constant and increase  $\Gamma$  from 0.25 to 3 in intervals of 0.25, while in the second we instead hold  $\Gamma = 1$  constant and increase  $\sigma_{\text{max}}$  from 0.025 to 0.25 in intervals of 0.025.

The black, red, and blue lines in Fig. 6 depict the relative errors  $\delta K(c)$ ,  $\delta K^1(c)$ , and  $\delta K^2(c)$ , respectively, in the case where  $\sigma_{\text{max}}$  is varied and  $\Gamma$  is held constant. In this case,  $\delta K(c)$  and  $\delta K^2(c)$  increase monotonically as  $\sigma_{\text{max}}$  increases, but  $\delta K^1(c)$  only increases until  $\sigma_{\text{max}} = 0.225$  after which it begins to decrease. Moreover, at the same point  $\delta K^2(c)$  becomes greater than  $\delta K^1(c)$  for the first time. This behavior arises because the magnitude of the  $\hat{r}_2$  component of the normal to the boundary,  $\hat{n}_{\text{out}}$ , increases with increasing  $\sigma_{\text{max}}$ , while the magnitude of the  $\hat{r}_1$  component decreases [see Eq. (2.25)]. Therefore, the flux over  $\partial\Omega_R$  in the  $\hat{r}_2$  direction increases, while the flux over this boundary in the  $\hat{r}_1$  direction decreases.

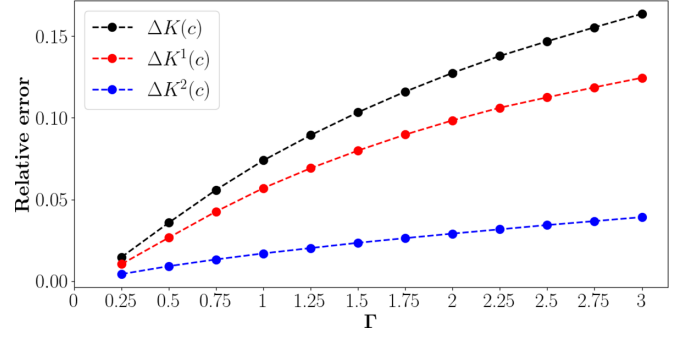


FIG. 7. The relative error between the steady-state reaction rate  $K_{\text{FE}}(c)$  from Eq. (4.8), and the approximate reaction rate  $K_1(c)$ , given by Eq. (2.27), calculated for  $c = 1$ ,  $\hat{D}_1 = 2$ ,  $\hat{D}_2 = 1.5$ , and  $\sigma_{\text{max}} = 0.1$ , while  $\Gamma$  is increased from 0.25 to 3 in intervals of 0.25. The steady-state reaction rate is defined as the total flux of the probability density over the boundary  $\partial\Omega_R$ , defined by Eq. (4.1). The black line shows the total relative error  $\delta K(c)$ , defined in Eq. (4.9a), between  $K_{\text{FE}}(c)$  and  $K_1(c)$ . This error arises because  $K_1(c)$  neglects  $O(\sigma_{\text{max}}^2)$  contributions to the flux over  $\partial\Omega_R$ . Since there are contributions of this order over  $\partial\Omega_R$  in both the  $\hat{r}_1$  and  $\hat{r}_2$  directions, we quantify them separately using the relative errors  $\delta K^1(c)$  and  $\delta K^2(c)$ , defined in Eqs. (4.9b) and (4.9c), and shown by the red and blue lines, respectively. That is,  $\delta K^1(c)$  and  $\delta K^2(c)$  represent the relative error that arises from ignoring  $O(\sigma_{\text{max}}^2)$  contributions to the flux over  $\partial\Omega_R$  in the  $\hat{r}_1$  and  $\hat{r}_2$  directions, respectively. The finite-element solution used to calculate  $K_{\text{FE}}(c)$  was evaluated over the domain  $\Omega_{\text{FE}} = \{(r_1, r_2) : \sigma_{\text{max}} \exp(\frac{-4\pi\Gamma r_2^2}{3}) \leq r_1 \leq 5, 0 \leq r_2 \leq 5\}$ .

Finally, recalling that  $K_1(c)$  is  $O(\sigma_{\text{max}})$ , we note that  $\delta K(c)$  growing linearly with  $\sigma_{\text{max}}$  indicates that the corrections to  $K_1(c)$  are  $O(\sigma_{\text{max}}^2)$  as expected.

Similarly, Fig. 7 displays the relative errors  $\delta K(c)$ ,  $\delta K^1(c)$ , and  $\delta K^2(c)$  as a black, red, and blue line, respectively, in the case where  $\Gamma$  is varied and  $\sigma_{\text{max}}$  is constant. The three relative errors increase monotonically, but the rate of increase appears to decrease as  $\Gamma$  increases. The height of  $\partial\Omega_R$  decays more rapidly as  $\Gamma$  increases, but the relationship between this parameter and  $\hat{n}_{\text{out}}$  is less straightforward. For any particular value of  $r_2$ , which defines a particular point on  $\partial\Omega_R$ , the magnitude of the  $\hat{r}_2$  ( $\hat{r}_1$ ) component of  $\hat{n}_{\text{out}}$  will initially increase (decrease) with increasing  $\Gamma$  until it reaches a local maximum (minimum) after which it begins to decrease (increase) as  $\Gamma$  increases further. Moreover, the value of  $\Gamma$  at which this stationary point occurs decreases as  $r_2$  increases. Therefore, for a fixed concentration and hence density profile, the approximation  $\hat{n}_{\text{out}} = -\hat{r}_1$  initially becomes worse as  $\Gamma$  increases from zero and the relative errors all increase accordingly. However, if  $\Gamma$  continues to increase, then eventually the magnitude of the  $\hat{r}_2$  component of  $\hat{n}_{\text{out}}$  in the region where the density is the most concentrated will begin to decay and  $\hat{n}_{\text{out}}$  begins to converge to  $-\hat{r}_1$  and so  $K_{\text{FE}}(c)$  begins to converge to  $K_1(c)$ . Therefore, the relative errors will initially increase, plateau, and eventually begin to decrease again once  $\Gamma$  becomes large enough.

## B. Reaction boundary corrections

To reproduce realistic chemical kinetics, particle-based simulations must accurately reproduce known reaction rates.

In other words, modellers typically begin with a desired reaction rate, which we denote  $K_D(c)$ , and then determine what reaction conditions should be imposed on the system to reproduce this rate. The expression for  $K_1(c)$  given in Eq. (2.27) is advantageous since it can be easily solved for the function  $f(r_2)$ , which defines  $\partial\Omega_R$ , via an inverse Laplace transform [50]. That is, it allows us to derive an analytic expression for the reaction boundary  $\partial\Omega_R$  that (approximately) matches a given rate  $K_1(c)$ . Thus, the obvious approach is to replace  $K_1(c)$  with the desired rate  $K_D(c)$  and determine the corresponding reaction boundary. However, our results demonstrate that deriving  $\partial\Omega_R$  in this way will result in a boundary that does not reproduce  $K_D(c)$  exactly. Instead, the simulated reaction rate (assuming that all other sources of error are negligible) will be given by Eq. (3.7). This is problematic since small changes in the reaction rate can drastically change the behavior of biochemical systems (for example, in systems that exhibit bistability and hysteresis [70,71]) and, for the specific form of  $\partial\Omega_R$  considered here, the relative error between  $K_1(c)$ —or in this case  $K_D(c)$ —and  $K_{FE}(c)$  becomes large as  $\sigma_{\max}$  or  $\Gamma$  increases. Therefore, we aim to adjust  $\partial\Omega_R$  so that the reaction rate it produces—quantified by  $K_{FE}(c)$ —more closely matches the desired rate  $K_D(c)$ . Moreover, since during a simulation  $\partial\Omega_R$  must be evaluated each time there is potential for a reaction to occur, we would like to retain an analytic expression for this boundary that is efficient to evaluate and seek to alter the parameters that define  $\partial\Omega_R$  rather than its functional form. This amounts to assuming that the functional form of  $K_{FE}(c)$  is well approximated by that of  $K_1(c)$ .

To demonstrate how to correct  $\partial\Omega_R$  in this manner we suppose that the desired reaction rate is given by

$$K_D(c) = \frac{4\pi\hat{D}_1\sigma_D c}{V_{FE}(c + \Gamma_D)}, \quad (4.10)$$

with  $\sigma_D = 0.1$  and  $\Gamma_D = 1$ . Using Eq. (2.27) we find that the boundary defined in Eq. (4.1) (approximately) matches this reaction rate. Therefore, we adopt this functional form for  $\partial\Omega_R$  and set  $\sigma_{\max} = 0.1$  and  $\Gamma = 1$ . In Fig. 8 we compare  $K_D(c)$  and  $K_{FE}(c)$  for this initial boundary in the case that  $\hat{D}_1 = 2$ ,  $\hat{D}_2 = 1.5$ , and  $c$  is increased from 1 to 20 in increments of 1. Figure 8(a) depicts  $K_D(c)$  and  $K_{FE}(c)$  using a blue line and the red points, respectively. The corresponding relative error,

$$\delta K_{FE}(c) = \frac{K_{FE}(c) - K_D(c)}{K_D(c)}, \quad (4.11)$$

is shown in Fig. 8(b) and decreases monotonically as  $c$  increases. This occurs because as  $c$  increases, the probability of finding the closest molecule of C close to the origin (at small  $r_2$ ) increases and the probability density profile narrows, which reduces the influence of the curvature of  $\partial\Omega_R$  on the reaction rate. In other words, as  $P_h$  becomes more localized the relevant part of  $\partial\Omega_R$  [in the region where  $4\pi r_2^2 P(r_1, r_2) > 0$ ] is better approximated by a constant. This means that  $K_{FE}(c)$  is well approximated by  $K_1(c)$  and therefore matches  $K_D(c)$  more closely since in this case  $K_D(c) = K_1(c)$ .

To better quantify the difference between  $K_{FE}(c)$  and  $K_D(c)$  across the range of concentrations considered we assume  $K_{FE}(c)$  is well approximated by the functional form of  $K_D(c)$ ,

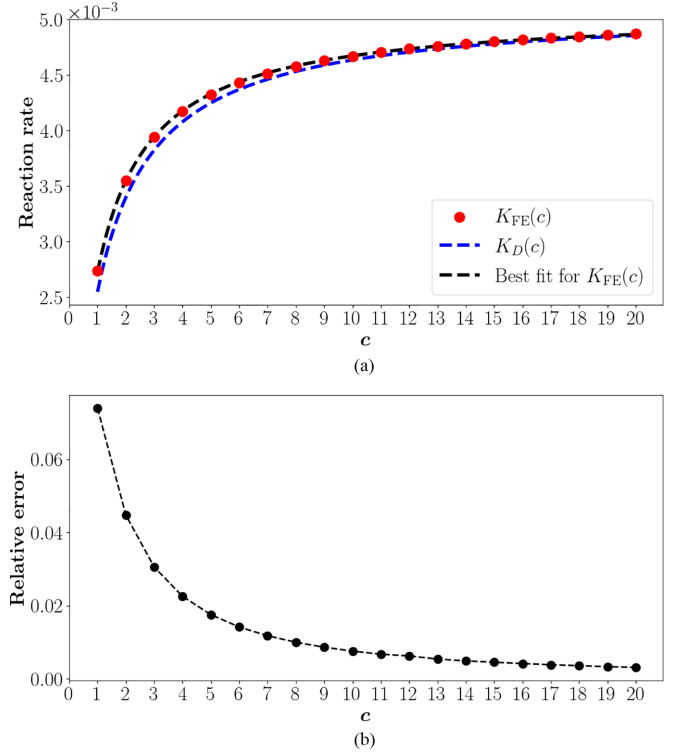


FIG. 8. The steady-state reaction rate  $K_{FE}(c)$  obtained from the finite-element solution via Eq. (4.8), for  $\sigma_{\max} = 0.1$ ,  $\Gamma = 1$ ,  $\hat{D}_1 = 2$ , and  $\hat{D}_2 = 1.5$ , while the concentration  $c$  is increased from 1 to 20 in increments of 1. The plot in (a) compares  $K_{FE}(c)$ , shown by the red points, to the desired reaction rate  $K_D(c)$  shown by the blue line and defined in Eq. (4.10) with  $\sigma_D = 0.1$  and  $\Gamma_D = 1$ . The black line shows the line of best fit for  $K_{FE}(c)$  when assuming the model in Eq. (4.12) and is defined by the parameters  $\sigma_E = 0.1$  and  $\Gamma_E = 0.86$ . The plot in (b) displays the relative error  $\delta K_{FE}(c)$ , defined in Eq. (4.11), between  $K_{FE}(c)$  and  $K_D(c)$  for the same set of parameters and shows that  $\delta K_{FE}(c)$  decreases monotonically as  $c$  is increased.

and fit the model

$$K_{FE}(c) = \frac{4\pi\hat{D}_1\sigma_E c}{V_{FE}(c + \Gamma_E)}, \quad (4.12)$$

to determine the “effective” parameters  $\sigma_E$  and  $\Gamma_E$ . If  $\partial\Omega_R$  reproduced the desired reaction rate exactly, then  $\sigma_E$  and  $\Gamma_E$  would be identical to  $\sigma_D$  and  $\Gamma_D$ , respectively. However, we already know that this is not the case here and the resulting line of best fit is defined by  $\sigma_E = 0.1$  and  $\Gamma_E = 0.86$  and is shown by the black dotted line in Fig. 8(a). Through this fit we can see that  $\sigma_D$  is well approximated by  $\sigma_E$ , but there is a large discrepancy between  $\Gamma_D$  and  $\Gamma_E$  with a corresponding relative error of 14%.

Our goal now is to alter  $\partial\Omega_R$ , by varying  $\sigma_{\max}$  and  $\Gamma$ , so that the error between  $K_{FE}(c)$  and  $K_D(c)$  is minimized. It is important to emphasize that  $K_D(c)$  is determined by the modeller and that our goal is to determine a reaction boundary that reproduces this rate. In contrast,  $K_1(c)$  and  $K_{FE}(c)$  both approximate the reaction rate associated with the current reaction boundary  $\partial\Omega_R$ . The former does so through Eq. (2.27), while the latter is connected to  $\partial\Omega_R$  through Eq. (4.8) and



serves as a proxy for the exact reaction rate  $K(c)$ . Crucially, altering  $\partial\Omega_R$  changes  $K_I(c)$  and  $K_{FE}(c)$  but not  $K_D(c)$ .

Since the error between  $K_D(c)$  and  $K_{FE}(c)$  depends on the concentration, we use the trust feigion feffective method developed by Branch *et al.* [72] to minimize the sum of squared residuals between these quantities. This method is available via the *least\_squares* function in the open-source SciPy library [73]. We define the residual for a given concentration as

$$r(c) = K_{FE}(c) - K_D(c), \quad (4.13)$$

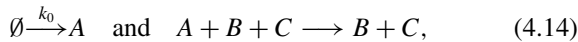
and recall that initially  $\sigma_{\max} = 0.1$  and  $\Gamma = 1$  define  $\partial\Omega_R$  through Eq. (4.1). In addition, we use Eq. (4.3) to derive an analytic approximation of the Jacobian for  $K_{FE}(c)$ . Each iteration of the algorithm we

- (1) construct a finite-element mesh  $\mathcal{T}_h$  according to the current values of  $\sigma_{\max}$  and  $\Gamma$ ;
- (2) compute  $K_{FE}(c)$ , increasing  $c$  from 1 to 20 in intervals of size 1;
- (3) update the values of the parameters  $\sigma_{\max}$  and  $\Gamma$ , thus defining the new boundary  $\partial\Omega_R$  and Jacobian for the next iteration.

This process is continued until the sum of the squares of the residuals or the values of  $\sigma_{\max}$  and  $\Gamma$  do not change significantly between successive iterations.

In our case, the optimization yields  $\sigma_{\max} = 0.10$  and  $\Gamma = 1.19$  and we compare  $K_{FE}(c)$  for this boundary to  $K_D(c)$  in Fig. 9. The blue line in Fig. 9(a) represents  $K_D(c)$ , the red points denote  $K_{FE}(c)$  calculated for the boundary in Eq. (4.1) defined by the optimized values of  $\sigma_{\max}$  and  $\Gamma$ , and the black line is the line of best fit through these points for the model in Eq. (4.12). The new line of best fit is defined by  $\sigma_E = 0.1$  and  $\Gamma_E = 1.01$ , which means that again  $\sigma_D$  is well approximated by  $\sigma_E$ , while the relative error between  $\Gamma_D$  and  $\Gamma_E$  has reduced in magnitude from 14% to just 1%. Similarly, Fig. 9(b) shows a reduction in the relative error between  $K_{FE}(c)$  and  $K_D(c)$  for  $c \leq 15$  while there is a slight increase in the error for  $c > 15$ . Finally, the sum of the squares of the residuals has been significantly reduced from  $2.5 \times 10^{-2}$  to  $1.5 \times 10^{-3}$ .

To demonstrate the effect of this correction in particle-based simulations, we use the algorithm developed by Kearney and Flegg [50] to simulate a system in which molecules of A, B, and C react according to



where  $k_0$  is a zeroth-order rate constant that controls the production of A, and the trimolecular degradation of A is governed by the reaction boundary in Eq. (4.1).

The initial number of A molecules ( $N_A$ ) is sampled from the corresponding steady-state distribution, which for this birth-death process is a Poisson distribution [74] with mean

$$E[N_A] = \frac{k_0 V_{PB}(c + \Gamma)}{4\pi \hat{D}_1 \sigma_{\max} bc}, \quad (4.15)$$

where  $V_{PB}$  is the volume of the simulation domain. The number of B molecules ( $N_B$ ) is chosen so that the concentration is  $b = N_B/V_{PB} = 1$ , while the number of C molecules is set to produce the desired concentration  $c$ . Setting  $k_0 = 1/V_{PB}$  allows the trimolecular degradation of A to be computed as

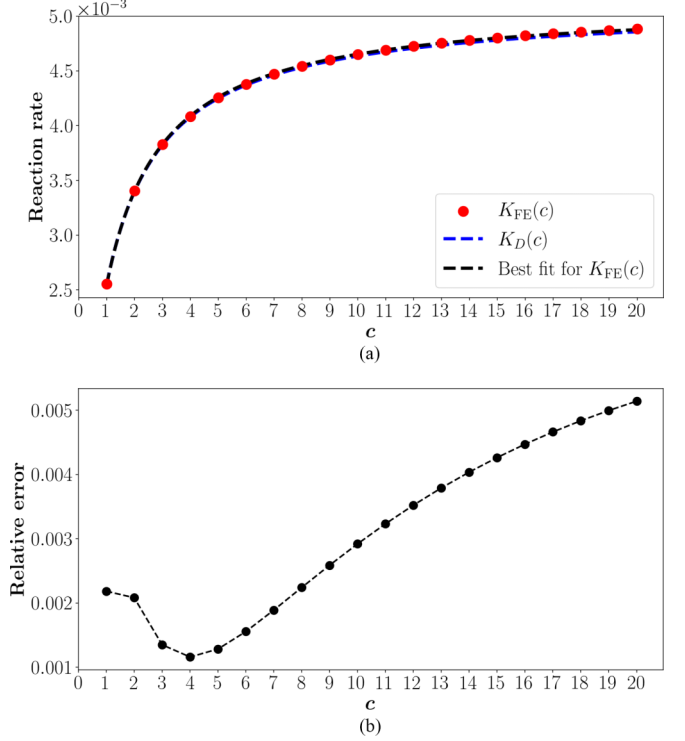


FIG. 9. The steady-state reaction rate  $K_{FE}(c)$ , computed via Eq. (4.8) using the corrected boundary defined by Eq. (4.1) with  $\sigma_{\max} = 0.1$  and  $\Gamma = 1.19$ . We consider  $\hat{D}_1 = 2$ ,  $\hat{D}_2 = 1.5$ , and  $c = 1$  to 20 in steps of 1 to match Fig. 8. In (a)  $K_{FE}(c)$ , shown by the red points, is compared to the desired reaction rate  $K_D(c)$ , shown by the blue line, and defined in Eq. (4.10) with  $\sigma_D = 0.1$  and  $\Gamma_D = 1$ . The black line shows the line of best fit for  $K_{FE}(c)$  assuming the model in Eq. (4.12) and is defined by the parameters  $\sigma_E = 0.1$  and  $\Gamma_E = 1.01$ . The plot in (b) displays the corresponding relative error  $\delta K_{FE}(c)$ , defined in Eq. (4.11), between  $K_{FE}(c)$  and  $K_D(c)$ . Compared to Fig. 8(b) we can see that the corrected boundary reduces the relative error for  $c \leq 15$ . However, now the relative error tends to increase with increasing  $c$  and is worse than it was previously for  $c > 15$ .

the inverse of  $E[N_A]$ , yielding the rate constant

$$k_{PB}(c) = \frac{1}{E[A]} = \frac{4\pi \hat{D}_1 \sigma_{\max} c}{c + \Gamma}, \quad (4.16)$$

which is related to the corresponding reaction rate by  $K_{PB}(c) = k_{PB}(c)/V_{PB}$ .

Notice that we have assumed that the volume of the particle-based simulation domain differs from  $V_{FE}$ . This is convenient because it allows us to assume that  $V_{PB}$  is an integer—we consider  $V_{PB} = 50$  here—which is helpful when setting reactant concentrations. Moreover, while  $V_{FE}$  must be large enough for the boundary conditions in Eqs. (3.11)–(3.13) to be valid, no such constraint applies to  $V_{PB}$ . Instead, because we impose periodic boundary conditions on the domain,  $V_{PB}$  only needs to be large enough to contain a sufficient number of C molecules for the probability density  $P(r_1, r_2)$ , which was derived in the limit that  $N_C \rightarrow \infty$  [see Eq. (2.13)], to serve as a good approximation for the distribution of the closest molecule of C to the center of diffusion of any pair of A and B molecules. Tests conducted by Kearney and Flegg [50] indicate that  $N_C \geq 50$  is sufficient.

TABLE I. The effect of correcting the reaction boundary  $\partial\Omega_R$  in particle-based simulations of Reaction (4.14). The steady-state rate constant  $k_{PB}(c)$  is computed using Eq. (4.16), where the mean of  $N_A$  is obtained from  $10^4$  simulation replicates for  $c = 1$  and  $c = 2$ , and from  $1.5 \times 10^4$  replicates for  $c = 4$ . The relative error,  $\delta k_{PB}(c)$ , between the simulated steady-state reaction rate and the desired reaction rate is calculated using Eq. (4.17). We also provide the relative error,  $\delta K_{FE}(c)$ —calculated from the finite-element solution using Eq. (4.11)—for comparison. Results are given for the reaction boundary in Eq. (4.1) both before and after the correction, defined by  $\sigma_{\max} = 0.1$ ,  $\Gamma = 1$  and  $\sigma_{\max} = 0.099$ ,  $\Gamma = 1.20$ , respectively. Here we consider  $\hat{D}_1 = 2$  and  $\hat{D}_2 = 5.5$ .

$c$	$k_{PB}(c)$	$\delta k_{PB}(c)$	$\delta K_{FE}(c)$
Uncorrected $\partial\Omega_R$ ( $\sigma_{\max} = 0.1$ , $\Gamma = 1$ )			
1	$1.37 \pm 0.02$	$0.091 \pm 0.013$	0.123
2	$1.80 \pm 0.02$	$0.075 \pm 0.014$	0.071
4	$2.06 \pm 0.02$	$0.024 \pm 0.012$	0.031
Corrected $\partial\Omega_R$ ( $\sigma_{\max} = 0.099$ , $\Gamma = 1.20$ )			
1	$1.28 \pm 0.01$	$0.019 \pm 0.011$	0.026
2	$1.67 \pm 0.02$	$-0.002 \pm 0.013$	0.006
4	$1.97 \pm 0.02$	$-0.018 \pm 0.011$	-0.011

All molecules are initially distributed uniformly at random throughout the simulation domain, and any molecule of A produced by the zeroth-order reaction also has its initial position chosen uniformly at random. The diffusion coefficients remain equal to one for A and B, but we increase the diffusion constant of C to  $D_2 = 5$ , so that  $\hat{D}_2 = 5.5$ . This increases the flux in the  $\eta_2$  direction and hence the magnitude of the error, allowing the correction to be resolved with fewer simulation replicates. However, this change only slightly alters the parameters for the corrected boundary, which is now defined by  $\sigma_{\max} = 0.099$  and  $\Gamma = 1.20$ . Dimensionless time steps of  $t_{\text{step}} = 10^{-6}$  are used to update the positions of the molecules, and the simulation is run until  $t = 20$ , after which the value of  $N_A$  is sampled. For each value of  $c \in \{1, 2, 4\}$  we perform  $10^4$ ,  $10^4$ , and  $1.5 \times 10^4$  replicates, respectively, and calculate  $k_{PB}(c)$  according to Eq. (4.16).

The results for both the original uncorrected reaction boundary ( $\sigma_{\max} = 0.1$  and  $\Gamma = 1$ ) and the corrected reaction boundary ( $\sigma_{\max} = 0.099$  and  $\Gamma = 1.20$ ) are shown in Table I. To compare  $k_{PB}(c)$  to the desired reaction rate  $K_D(c)$ , with  $\sigma_D = 0.1$  and  $\Gamma_D = 1$ , we calculate the relative error

$$\delta k_{PB}(c) = \frac{k_{PB}(c) - V_{FE}K_D(c)}{V_{FE}K_D(c)}, \quad (4.17)$$

which we then compare to the corresponding relative error,  $\delta K_{FE}(c)$ , obtained using the finite-element solution.

The boundary correction significantly reduces the magnitude of  $\delta k_{PB}(c)$  for all concentrations considered, and the sum of the squares of the residuals has been reduced from  $(3.2 \pm 0.7) \times 10^{-2}$  to  $(2 \pm 2) \times 10^{-3}$ .

## V. DISCUSSION

The leading-order solution  $P_0$  to the steady-state probability density in Eq. (2.24) corresponds to the exact solution

in the case that  $\partial\Omega_R$  is independent of  $r_2$ , that is, if  $f(r_2)$  is a constant. This simplifies the problem significantly since the probability of finding the state associated with the closest molecule of C with a given  $r_1$  is independent of the probability of finding the same state with a particular  $r_2$ . In other words, in this case, Eq. (2.19) is separable. However, this simple boundary is equivalent to imposing Smoluchowski's reaction condition on Reaction (1.5) and therefore only yields bimolecular mass-action kinetics. To obtain more complex kinetics, in general  $\partial\Omega_R$  will need to be spatially dependent, and a separable solution cannot be found. The degree to which the exact density can be approximated by  $P_0$  depends on how well  $\partial\Omega$  is approximated by the flat boundary assumed when deriving  $P_0$ . This dependence can be inferred from Fig. 7 which shows that the steady-state reaction rate  $K_{FE}(c)$  converges to the approximate rate  $K_1(c)$ , which is constructed from  $P_0$ , as  $\Gamma$  reduces since in the limit that  $\Gamma \rightarrow 0$  the boundary becomes constant.

The approximate steady-state reaction rate  $K_1(c)$  neglects  $O(\sigma_{\max}^2)$  contributions to the total flux over  $\partial\Omega_R$ , which amounts to ignoring the  $O(\sigma_{\max}^2)$  corrections to  $P_0$  and the flux of the probability density over  $\partial\Omega_R$  in the  $\hat{r}_2$  direction. In essence, we ignore the diffusive and advective flux of the density in the  $\hat{r}_2$  direction and we also neglect any influence this diffusive and advective motion has on the probability density itself. As a consequence, compared to  $P_h$ ,  $P_0$  underestimates the probability that the closest molecule is close to the origin, see Fig. 4, while  $K_1(c)$  underestimates the contributions of the flux over  $\partial\Omega_R$  in both the  $\hat{r}_1$  and  $\hat{r}_2$  directions, see Figs. 6 and 7. Both corrections to  $K_1(c)$  are  $O(\sigma_{\max}^2)$  but we find that the correction to the flux over  $\partial\Omega_R$  in the  $\hat{r}_1$  direction is typically larger in magnitude. Although, as shown in Fig. 6, this is parameter dependent, and it is possible for the correction in the  $\hat{r}_2$  direction to be larger.

Kearney and Flegg [50] also examined the relative error between  $K(c)$  and  $K_1(c)$  for the particular choice of  $\partial\Omega_R$  given in Eq. (4.1). However, they approximated  $K(c)$  using the reaction rate obtained from a particle-based simulation of Reaction (1.5) rather than  $K_{FE}(c)$ . As a result, for comparable parameter choices, our values for  $\delta K(c)$  do not agree with those reported by Kearney and Flegg. In particular, for  $c = 10$ ,  $\sigma_{\max} = 0.1$ ,  $\Gamma = 1$ ,  $\hat{D}_1 = 2$ , and  $\hat{D}_2 = 1.5$ , while Kearney and Flegg report a (signed) relative error of less than  $-2.5 \times 10^{-2}$  indicating that the simulated rate is less than  $K_1(c)$ . In comparison, for this choice of parameters, we find that  $K_{FE}(c)$  exceeds  $K_1(c)$  and that  $\delta K(c) = 7.6 \times 10^{-3}$ . In fact, for all parameter combinations considered, we find that the relative error is strictly positive, suggesting that  $K_1(c)$  underestimates the true reaction rate.

This disparity arises because the particle-based simulation developed by Kearney and Flegg underestimates the true reaction rate. This occurs because it does not exactly produce the underlying particle dynamics, allowing some reactions to go undetected. The resulting discrepancy is evident in Table I, where  $\delta k_{PB}(c)$  underestimates the expected relative error given by  $\delta K_{FE}(c)$  for the uncorrected boundary when  $c = 1$ . Although increasing the height of the reaction boundary has been shown to mitigate this issue, we have not applied this adjustment because it would obscure the high-order corrections studied here. Fortunately, such limitations can be

overcome using more accurate simulation techniques [43,44], leaving only the error that arises from using  $K_1(c)$  to approximate the reaction rate.

In Sec. IV B we demonstrate how to minimize this source of error by altering the reaction boundary  $\partial\Omega_R$ . To obtain an analytic expression for  $\partial\Omega_R$ , we use Eq. (2.27) and the inverse Laplace transform to derive a boundary that (approximately) matches the desired reaction rate  $K_D(c)$ . This assumes that  $K_1(c)$  approximates the exact reaction rate, for which  $K_{FE}(c)$  is a proxy, well enough that the corresponding boundary is close enough to the true boundary that reproduces  $K_D(c)$  to serve as a good starting point for the optimization. To retain an analytic expression for  $\partial\Omega_R$  we choose to only alter the parameters,  $\sigma_{\max}$  and  $\Gamma$  in our case, that define the boundary during the optimization rather than the functional form of the boundary itself. In essence, we are assuming that the true boundary that corresponds to  $K_D(c)$  has the same functional form as the initial boundary determined using Eq. (2.27). This is equivalent to assuming that  $K_{FE}(c)$  for a given  $\partial\Omega_R$  has the same dependence on the concentration  $c$  as the approximation  $K_1(c)$ , and only the dependence on the boundary parameters differs between the two rates.

Our approach is simple to implement because it relies on the open-source library SciPy, and the optimized boundary is no more difficult to evaluate than the initial boundary. This is particularly important for the efficiency of particle-based simulations, since the value of reaction boundary must be evaluated for each potential reaction event. The corrections can be precomputed for any given chemical system and could be tabulated for common reaction rates to reduce unnecessary computation. Moreover, our results in Table I, demonstrate that such corrections can be applied in practice to improve the accuracy of particle-based simulations.

However, notice that if the concentration is large, then altering  $\partial\Omega_R$  can increase rather than decrease the relative error between  $K_{FE}(c)$  and  $K_D(c)$ . As shown in Fig. 8, for the initial boundary, determined by Eq. (2.27),  $K_{FE}(c)$  will converge to  $K_D(c)$  as  $c$  increases. This is because as  $c$  increases the probability density becomes more localized in  $r_2$  and the likelihood of finding the closest molecule near the origin (at small  $r_2$ ) increases. Therefore, the portion of  $\partial\Omega_R$  over which the flux of the probability density is nonzero continually decreases and becomes localized to small values of  $r_2$ . Eventually, the relevant portion of  $\partial\Omega_R$  given in Eq. (4.1) can be considered essentially constant and, under such conditions,  $K_{FE}(c)$  is equal to  $K_1(c)$ . That is, for sufficiently large concentrations, Eq. (2.27) yields the correct reaction boundary for the kinetics considered here. Since our approach seeks to minimize the sum of the squares of the residuals across a range of concentrations, the optimization that will typically improve the error where it is initially large and will potentially make the error worse where it is initially small.

It may be possible to achieve better convergence to the desired reaction rate by allowing the functional form of  $\partial\Omega_R$  to be varied during the optimization. An obvious starting point in this direction would be to model the concentration dependence of the error between  $K_{FE}(c)$  and  $K_D(c)$  and then attempt to introduce additional terms to the reaction boundary that account for the differing concentration dependence of  $K_{FE}(c)$  and  $K_1(c)$ . Furthermore, if we abandon our attachment

to a simple analytic expression for  $\partial\Omega_R$ , then one could selectively alter portions of the boundary using machine learning techniques to improve the error for selected values of  $c$ , while minimizing the adverse effects for concentrations outside this range. Finally, if the range of  $c$  can be estimated in advance, then better results can be obtained by performing the optimization over this application-specific range. However, there exist many biochemical systems in which the concentration of reactants undergo large-scale oscillations [75–77] for which this will not be possible.

## VI. CONCLUSION

We considered the evolution of a system that consists of diffusing molecules from three different chemical species labeled A, B, and C. The molecules react whenever the distance  $r_1$  between two molecules of A and B is less than or equal to a function  $f(r_2)$  of the distance  $r_2$  to the closest molecule of C. This proximity-based reaction condition defines a reactive region in the state space of the system on whose surface ( $\partial\Omega_R$ ) triplets of molecules, where each triplet contains one molecule of A, B, and C, are absorbed. We derive a non-linear partial integrodifferential equation, Eq. (2.19), which describes the evolution of the probability density to find the closest molecule, relative to a particular pair of A and B molecules, of C at a given position. The proximity-based reaction condition is imposed as an absorbing boundary condition on the governing equation, see Eq. (2.21), and the total flux of the probability density over this boundary corresponds to the reaction rate for the system.

By assuming that  $\partial\Omega_R$  extends a small distance  $\sigma_{\max}$  in the  $\hat{r}_1$  direction, we use singular perturbation theory to derive a leading-order solution ( $P_0(r_1, r_2)$ ) for the steady-state probability density. This solution is then used to construct an approximation,  $K_1(c)$  defined in Eq. (2.27), to the steady-state reaction rate for the system. Both  $P_0$  and  $K_1(c)$  neglect corrections of  $O(\sigma_{\max}^2)$ , which are difficult to study analytically, so we construct finite-element solutions  $P_h$  and  $s_h$  for the probability density and the flux of this density respectively, for the specific choice of  $\partial\Omega_R$  defined in Eq. (4.1). Using these solutions, we show that  $P_0$  underestimates the probability of finding the closest molecule of C near the origin, or at small  $r_2$  values as shown in Fig. 4, while  $K_1(c)$  underestimates the reaction rate  $K_{FE}(c)$  obtained from  $s_h$ ; see Figs. 6, 7, and 8.

This is the first time such errors have been quantified, and our results elucidate the source of the errors reported in particle-based simulations of an equivalent system [50]. In Sec. IV B we demonstrate how to correct for these errors in a manner that can be easily and efficiently incorporated into existing simulations. Moreover, our work provides insight into the dynamics of particles within particle-based simulations and should assist in the continual development of novel proximity-based reaction conditions. Although we have only considered a single functional form for  $\partial\Omega_R$ , our analysis could be extended to other reactive boundaries. So long as the boundary remains monotonically decreasing in  $r_2$  as assumed here, our analysis should extend in a straightforward manner. Violating this assumption complicates matters as the state associated with the closest molecule of C will not necessarily cross the boundary first. If we mandate that reactions only

occur when this specific state crosses the boundary, then the dynamics of the system will still be governed by Eq. (2.19), but we would expect the behavior of the examined errors to change since the normal vector to the boundary will sometimes have a component in the opposite direction of  $\hat{\mathbf{r}}_2$ . In these regions, the advective motion described by the final term in Eq. (2.19) will push the relevant state away from the reaction boundary, thus decreasing the reaction rate as opposed to always increasing the rate as is the case for a monotonically decreasing boundary.

### ACKNOWLEDGMENTS

This work has been partially supported by the Australian Research Council through the Future Fellowship Grant No. FT220100496 and Discovery Project Grant No. DP22010316.

### DATA AVAILABILITY

The data that support the findings of this article are openly available [79].

### APPENDIX A: THE EVOLUTION OF $\Phi(\eta_2, t)$

To derive the governing equation for  $\Phi(\eta_2, t)$ , we consider  $\mathcal{L}_2\Phi(\eta_2, t)$  where

$$\mathcal{L}_2 \equiv \frac{\partial}{\partial t} - \hat{D}_2 \hat{\nabla}_2^2, \quad (\text{A1})$$

is the diffusion operator on the three-dimensional space spanned by  $\eta_2$ , originally given in Eq. (2.7a). The time derivative of  $\Phi(\eta_2, t)$  is given by

$$\Phi_t = g\phi_t - c\phi g \int_{V_2} \phi_t(\eta'_3, t) dV'_2, \quad (\text{A2})$$

where we have used the  $t$  subscript to denote differentiation with respect to time and defined

$$g \equiv g(\eta_2, t) = \exp\left(-c \int_{V_2} \varphi(\eta'_2, t) dV'_2\right), \quad (\text{A3})$$

for notational convenience. We can also take the Laplacian of  $\Phi$  with respect to the coordinates of  $\eta_2$

$$\hat{\nabla}_2^2 \Phi = g \hat{\nabla}_2^2 \phi + 2(\hat{\nabla}_2 \phi) \cdot (\hat{\nabla}_2 g) + \phi \hat{\nabla}_2^2 g, \quad (\text{A4})$$

which when combined with Eq. (A2) yields

$$\begin{aligned} \mathcal{L}_2 \Phi &= g\phi_t - c\phi g \int_{V_2} \phi_t(\eta'_3, t) dV'_2 \\ &\quad - \hat{D}_2 [g \hat{\nabla}_2^2 \phi - 2(\hat{\nabla}_2 \phi) \cdot (\hat{\nabla}_2 g) - \phi \hat{\nabla}_2^2 g]. \end{aligned} \quad (\text{A5})$$

Recalling that  $\mathcal{L}_2 \phi = 0$  from Eq. (2.7a) and applying the divergence theorem we find

$$\begin{aligned} \mathcal{L}_2 \Phi &= \hat{D}_2 \left[ -c\phi g \int_{V_2} \hat{\nabla}_2^2 \phi(\eta'_3, t) dV'_2 \right. \\ &\quad \left. - 2(\hat{\nabla}_2 \phi) \cdot (\hat{\nabla}_2 g) - \phi \hat{\nabla}_2^2 g \right] \\ &= -c\hat{D}_2 \phi g \oint_{S_2} (\hat{\nabla}_2 \phi(\eta'_3, t)) \cdot \hat{\mathbf{r}}_2 dA'_2 \\ &\quad - 2\hat{D}_2 (\hat{\nabla}_2 \phi) \cdot (\hat{\nabla}_2 g) - \hat{D}_2 \phi \hat{\nabla}_2^2 g, \end{aligned} \quad (\text{A6})$$

where  $S_2$  is the surface of a sphere of radius  $r_2 = \|\eta_2\|$ ,  $dA'_2$  is an elemental area on that surface and  $\hat{\mathbf{r}}_2$  is the unit outward facing normal vector. The diffusion in the  $\eta_2$  coordinate is isotropic, and so  $\phi$  is independent of orientation. That is,  $\phi$  only has radial dependence, so we have

$$\begin{aligned} \hat{\nabla}_2 g &= \hat{\nabla}_2 \exp\left(-c \int_{V_2} \varphi(\eta'_2, t) dV'_2\right) \\ &= -cg\phi \left( \oint_{S_2} dA'_2 \right) \hat{\mathbf{r}}_2. \end{aligned} \quad (\text{A7})$$

By the same reasoning we are able to take the integrand outside the integral in Eq. (A6) and by substituting in Eq. (A7) we obtain

$$\begin{aligned} \mathcal{L}_2 \Phi &= -\hat{D}_2 [(\hat{\nabla}_2 \phi) \cdot (\hat{\nabla}_2 g) + \phi \hat{\nabla}_2^2 g] \\ &= -\hat{D}_2 \hat{\nabla}_2 \cdot (\phi \hat{\nabla}_2 g) \\ &= \hat{D}_2 \hat{\nabla}_2 \cdot \left( cg\phi^2 \left( \oint_{S_2} dA'_2 \right) \hat{\mathbf{r}}_2 \right) \\ &= \hat{D}_2 \hat{\nabla}_2 \cdot (4\pi r_2^2 c\phi \hat{\mathbf{r}}_2). \end{aligned} \quad (\text{A8})$$

That is,

$$\frac{\partial \Phi(\eta_2, t)}{\partial t} = \hat{D}_2 \hat{\nabla}_2^2 \Phi(\eta_2, t) + \hat{D}_2 \hat{\nabla}_2 \cdot (4\pi r_2^2 c\phi \Phi(\eta_2, t) \hat{\mathbf{r}}_2), \quad (\text{A9})$$

as stated in Eq. (2.14).

### APPENDIX B: SINGULAR PERTURBATION ANALYSIS

To determine the steady-state solution  $P(r_1, r_2)$  of Eq. (2.19) near the reaction boundary  $\partial\Omega_R$ , defined in Eq. (2.5), we seek a radial steady-state solution,  $\bar{P}(u_1, u_2) = P(r_1, r_2)$ , where

$$u_1 = \frac{r_1}{\sigma_{\max}} \quad \text{and} \quad u_2 = r_2, \quad (\text{B1})$$

are scaled radial coordinates. With this change of variables, the steady-state form of Eq. (2.19) becomes

$$\begin{aligned} \frac{\hat{D}_1}{u_1^2} \frac{\partial}{\partial u_1} \left( u_1^2 \frac{\partial \bar{P}(u_1, u_2)}{\partial u_1} \right) &+ \frac{\sigma_{\max}^2 \hat{D}_2}{u_2^2} \frac{\partial}{\partial u_2} \\ &\times \left( u_2^2 \frac{\partial \bar{P}(u_1, u_2)}{\partial u_2} + \frac{u_2^4 (\bar{P}(u_1, u_2))^2}{\int_{u_2}^{\infty} \bar{P}(u_1, u'_2) u_2'^2 du'_2} \right) = 0, \end{aligned} \quad (\text{B2})$$

while the associated boundary conditions are as follows:

$$\bar{P}(u_1, u_2) = 0 \quad \text{on} \quad u_1 = F(u_2),$$

$$\text{where } F(u_2) = \frac{f(u_2)}{\sigma_{\max}}, \quad (\text{B3a})$$

$$\lim_{u_1 \rightarrow \infty} \bar{P}(u_1, u_2) = \frac{c}{V} \exp\left(\frac{-4\pi c u_2^3}{3}\right), \quad (\text{B3b})$$

$$\lim_{u_2 \rightarrow \infty} \bar{P}(u_1, u_2) = \lim_{u_2 \rightarrow \infty} \frac{c}{V} \exp\left(\frac{-4\pi c u_2^3}{3}\right) = 0 \quad \text{and} \quad (\text{B3c})$$

$$\frac{\partial \bar{P}(u_1, u_2)}{\partial u_2} = 0, \quad \text{when } u_2 = 0. \quad (\text{B3d})$$



Following the change of variables the singular nature of the PDE becomes plain. Very close to  $\partial\Omega_R$  diffusion in the  $\hat{\mathbf{r}}_1$  direction dominates and there is comparatively little diffusive or advective motion in the  $\hat{\mathbf{r}}_2$  direction, where  $\hat{\mathbf{r}}_i$  is the unit radial basis vector for  $\boldsymbol{\eta}_i$ . In the limit that  $\sigma_{\max} \rightarrow 0$ , motion in the  $\hat{\mathbf{r}}_2$  direction can be ignored, and it is only necessary to consider diffusive flux in the  $\hat{\mathbf{r}}_1$  direction.

More formally, we assume the solution to Eq. (B2) can be expanded in a perturbation series of the form

$$\bar{P}(u_1, u_2) = \bar{P}_0(u_1, u_2) + \sigma_{\max}^2 \bar{P}_1(u_1, u_2) + O(\sigma_{\max}^4). \quad (\text{B4})$$

To derive the leading-order solution we substitute this perturbation series into Eq. (B2) and match the  $O(1)$  terms which leads to

$$\bar{P}_0(u_1, u_2) = h_0(u_2) \left( 1 - \frac{F(u_2)}{u_1} \right), \quad (\text{B5})$$

where  $h_0$  is an arbitrary function of  $u_2$ . To determine  $h_0$  we use the matching condition

$$\lim_{u_1 \rightarrow \infty} \bar{P}_0(u_1, u_2) = \frac{c}{V} \exp\left(\frac{-4\pi c u_2^3}{3}\right), \quad (\text{B6})$$

which yields

$$\bar{P}_0(u_1, u_2) = \frac{c}{V} \exp\left(\frac{-4\pi c u_2^3}{3}\right) \left( 1 - \frac{F(u_2)}{u_1} \right), \quad (\text{B7})$$

and amounts to requiring that in the bulk, far from  $\partial\Omega_R$ , the absorption of states on  $\partial\Omega_R$  causes a negligible perturbation in the solution. Finally, reverting to our original coordinates  $r_1$  and  $r_2$  we recover the approximate steady-state solution

$$P_0(r_1, r_2) = \frac{c}{V} \exp\left(\frac{-4\pi c r_2^3}{3}\right) \left( 1 - \frac{f(r_2)}{r_1} \right),$$

stated in Eq. (2.24) of the main text.

The results presented in the main text indicate that  $P_0$  is indeed the dominant term in the perturbation expansion of  $P$ . However, as shown below, the standard expansion in Eq. (B4) cannot be used to obtain higher-order corrections to the solution. Instead, these corrections have been quantified using finite-element methods, as detailed in the main text.

In an attempt to determine the  $O(\sigma_{\max}^2)$  correction to the solution we once again substitute the perturbation series into Eq. (B2) only now we match terms to  $O(\sigma_{\max}^2)$  to obtain

$$\begin{aligned} & \frac{\hat{D}_1}{u_1^2} \frac{\partial}{\partial u_1} \left( u_1^2 \frac{\partial \bar{P}_1(u_1, u_2)}{\partial u_1} \right) + \frac{\hat{D}_2}{u_2^2} \frac{\partial}{\partial u_2} \\ & \times \left( u_2^2 \frac{\partial \bar{P}_0(u_1, u_2)}{\partial u_2} + \frac{u_2^4 (\bar{P}_0(u_1, u_2))^2}{\int_{u_2}^{\infty} \bar{P}_0(u_1, u'_2) u_2'^2 du'_2} \right) = 0. \end{aligned} \quad (\text{B8})$$

To arrive at Eq. (B8) we have used the fact that

$$\frac{\hat{D}_1}{u_1^2} \frac{\partial}{\partial u_1} \left( u_1^2 \frac{\partial \bar{P}_0(u_1, u_2)}{\partial u_1} \right) = 0, \quad (\text{B9})$$

and performed a Taylor series expansion about  $\sigma_{\max}^2 = 0$  to write

$$\begin{aligned} & \frac{1}{\int_{u_2}^{\infty} (\bar{P}(u_1, u'_2)) u_2'^2 du'_2} \\ & = \frac{1}{I_0(u_2)} \frac{1}{1 + \frac{\sigma_{\max}^2}{I_0(u_2)} (I_1(u_2) + O(\sigma_{\max}^2))} \end{aligned} \quad (\text{B10})$$

$$= \frac{1}{I_0(u_2)} \left( 1 - \sigma_{\max}^2 \frac{I_1(u_2)}{I_0(u_2)} + O(\sigma_{\max}^4) \right), \quad (\text{B11})$$

where  $I_i(u_2) = \int_{u_2}^{\infty} (\bar{P}_i(u_1, u'_2)) u_2'^2 du'_2$ . To satisfy the condition in Eq. (B3a) we require

$$\bar{P}_1(u_1, u_2) = 0 \quad \text{on} \quad u_1 = F(u_2), \quad (\text{B12})$$

and the corresponding solution is

$$\begin{aligned} \bar{P}_1(u_1, u_2) = & \left( \int_{F(u_2)}^{u_1} \left( 1 - \frac{\xi}{u_1} \right) \xi \mathcal{L}_{u_2} \bar{P}_0(\xi, u_2) d\xi \right. \\ & \left. + h_1(u_2) \left( 1 - \frac{F(u_2)}{u_1} \right) \right), \end{aligned} \quad (\text{B13})$$

where

$$\begin{aligned} \mathcal{L}_{u_2} \bar{P}_0(u_1, u_2) \equiv & -\frac{\hat{D}_2}{\hat{D}_1 u_2^2} \frac{\partial}{\partial u_2} \left( u_2^2 \frac{\partial \bar{P}_0(u_1, u_2)}{\partial u_2} \right. \\ & \left. + \frac{u_2^4 (\bar{P}_0(u_1, u_2))^2}{\int_{u_2}^{\infty} \bar{P}_0(u_1, u'_2) u_2'^2 du'_2} \right), \end{aligned} \quad (\text{B14})$$

ultimately depends on the reaction boundary  $\partial\Omega_R$  and can be computed using Eq. (B7).

The arbitrary function  $h_1(u_2)$  is determined by the matching condition

$$\lim_{u_1 \rightarrow \infty} \bar{P}_1(u_1, u_2) = 0, \quad (\text{B15})$$

which is required to satisfy Eq. (B3b). This condition can only be satisfied, by choosing  $h_1$  appropriately, if the integral in Eq. (B13) remains bounded as  $u_1 \rightarrow \infty$ . In general, however, this integral diverges in the limit  $u_1 \rightarrow \infty$  because the term  $\xi \mathcal{L}_{u_2} \bar{P}_0(\xi, u_2)$  tends to infinity as  $\xi \rightarrow \infty$ . An exception arises when the leading-order solution  $\bar{P}_0$  is also a solution to the homogeneous equation associated with the differential operator  $\mathcal{L}_{u_2}$ , as occurs, for example, when  $\partial\Omega_R$ —and hence  $F(r_2)$ —is constant. In that case,  $\bar{P}_1$  vanishes identically since  $\bar{P}_0$  is the exact solution to the original PDE in Eq. (B2). The failure to satisfy the matching condition in the general case indicates that the assumed form of the perturbation series in Eq. (B4) is not appropriate beyond  $O(1)$ .

## APPENDIX C: FINITE-ELEMENT DISCRETISATION

All routines described in this Appendix have been implemented using the open-source finite-element library FEniCS [78], and a publicly available repository [79] contains the main codes required to reproduce the simulations presented in Sec. IV.

Before stating the finite-element formulation of Eq. (3.4), let us recall, for a sufficiently smooth vector-valued function  $\boldsymbol{\tau} = (\tau_1, \tau_2)^T$  and a scalar function  $v$ , the following integration

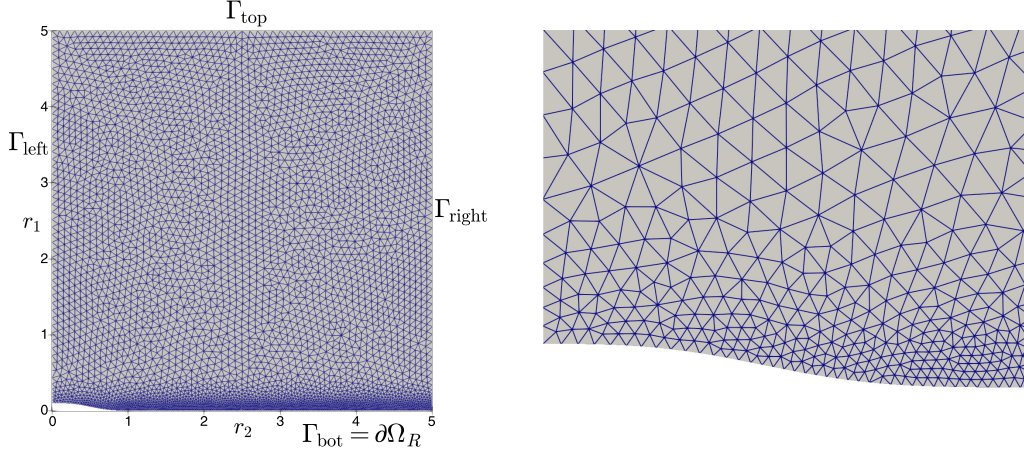


FIG. 10. Unstructured triangular mesh and boundary configuration of the computational domain (left), and zoom into the bottom left corner showing the mesh refinement near the absorbing boundary (right panel).

by parts formula for radial coordinates. This employs the two-dimensional gradient from Eq. (3.2), usual two-dimensional divergence  $\nabla_c \cdot \boldsymbol{\tau} = \partial_{r_1} \tau_1 + \partial_{r_2} \tau_2$ , radial divergence from Eq. (3.6) (noting that  $\nabla \cdot \boldsymbol{\tau} = \nabla_c \cdot \boldsymbol{\tau} + \frac{2}{r_1} \tau_1 + \frac{2}{r_2} \tau_2$ ), and usual integration by parts in two-dimensions:

$$\begin{aligned}
 & \int_{\Omega_{\text{FE}}} (\nabla \cdot \boldsymbol{\tau})(v\omega) dr_2 dr_1 \\
 &= \int_{\Omega_{\text{FE}}} (\nabla_c \cdot \boldsymbol{\tau})(v\omega) dr_2 dr_1 + \int_{\Omega_{\text{FE}}} 2 \left( \frac{\omega}{r_1} \tau_1 + \frac{\omega}{r_2} \tau_2 \right) v dr_2 dr_1 \\
 &= \int_{\partial\Omega_{\text{FE}}} (\boldsymbol{\tau} \cdot \mathbf{n})(v\omega) ds - \int_{\Omega_{\text{FE}}} (\boldsymbol{\tau} \cdot \nabla v) \omega dr_2 dr_1 \\
 &\quad - \int_{\Omega_{\text{FE}}} (\boldsymbol{\tau} \cdot \nabla \omega) v dr_2 dr_1 + \int_{\Omega_{\text{FE}}} 2 \left( \frac{\omega}{r_1} \tau_1 + \frac{\omega}{r_2} \tau_2 \right) v dr_2 dr_1 \\
 &= \int_{\partial\Omega_{\text{FE}}} (\boldsymbol{\tau} \cdot \mathbf{n})(v\omega) ds - \int_{\Omega_{\text{FE}}} (\boldsymbol{\tau} \cdot \nabla v) \omega dr_2 dr_1. \quad (\text{C1})
 \end{aligned}$$

Here  $\omega = (4\pi r_1 r_2)^2$  denotes the weight associated with the radial coordinates  $r_1$  and  $r_2$ , while  $\partial\Omega_{\text{FE}}$  denotes the boundary of  $\Omega_{\text{FE}}$  which we divide into four segments:  $\Gamma_{\text{left}}$ ,  $\Gamma_{\text{bot}}$ ,  $\Gamma_{\text{right}}$ , and  $\Gamma_{\text{top}}$ , defined by the regions  $r_2 = 0$ ,  $r_1 = f(r_2)$ ,  $r_2 = r_2^{\text{max}}$ , and  $r_1 = r_1^{\text{max}}$ , respectively. A sketch of an unstructured triangular mesh having more refinement near the absorbing boundary  $\Gamma_{\text{bot}} = \partial\Omega_R$ , and identifying all sub-boundaries is shown in Fig. 10.

Consider now a finite-element mesh  $\mathcal{T}_h$ —an unstructured partition of the domain  $\Omega_{\text{FE}}$  into triangles  $K$ —of maximum diameter  $h = \{\max h_K : K \in \mathcal{T}_h\}$ . Let us denote by  $\mathcal{E}_h$  the set of all interior edges  $e$  with length  $h_e$  (and  $\mathcal{E}_h^\partial$  denotes the boundary edges). In addition, we use  $\llbracket s \rrbracket_e$  to denote the jump of a scalar field  $s$  across the edge  $e$ . Proceeding from a weak formulation of (3.4) (derived from the integration by parts in radial coordinates (C1) and using the mixed type boundary conditions—for the flux essentially, and for the density and density moment naturally) and considering a mixed-primal Galerkin discretization, the finite-element formulation consists in finding the approximate unknowns of flux  $s_h$ , density

$P_h$ , and density moment  $Q_h$  in the discrete spaces  $\Sigma_h \times \Phi_h \times \Psi_h$ , such that

$$\begin{aligned}
 & \int_{\Omega_{\text{FE}}} s_h \cdot D\boldsymbol{\tau}_h \omega dr_2 dr_1 - \int_{\Omega_{\text{FE}}} P_h \nabla \cdot (D\boldsymbol{\tau}_h) \omega dr_2 dr_1 \\
 & \quad + \int_{\Omega_{\text{FE}}} \left( \frac{r_2^2 P_h^2}{Q_h} \hat{\mathbf{r}}_2 \right) \cdot (D\boldsymbol{\tau}_h) \omega dr_2 dr_1 \\
 &= - \int_{\Gamma_{\text{right}}} P_{\text{right}} D\boldsymbol{\tau}_h \cdot \mathbf{n} \omega ds - \int_{\Gamma_{\text{bot}}} P_{\text{bot}} D\boldsymbol{\tau}_h \cdot \mathbf{n} \omega ds \\
 & \quad - \int_{\Gamma_{\text{top}}} P_{\text{top}} D\boldsymbol{\tau}_h \cdot \mathbf{n} \omega ds \quad \forall \boldsymbol{\tau}_h \in \Sigma_h^0, \quad (\text{C2a})
 \end{aligned}$$

$$- \int_{\Omega_{\text{FE}}} v_h \nabla \cdot (Ds_h) \omega dr_2 dr_1 = 0 \quad \forall v_h \in \Phi_h, \quad (\text{C2b})$$

$$\begin{aligned}
 & \int_{\Omega_{\text{FE}}} (r_2^2 P_h - \nabla \cdot \hat{\mathbf{r}}_2 Q_h) w_h \omega dr_2 dr_1 \\
 & \quad - \int_{\Omega_{\text{FE}}} (\nabla w_h \cdot \hat{\mathbf{r}}_2) Q_h \omega dr_2 dr_1 + \int_{\Gamma_{\text{left}}} \hat{\mathbf{r}}_2 \cdot \mathbf{n} Q_h w_h \omega ds \\
 & \quad + \sigma_{\text{stab}} \sum_{e \in \mathcal{E}_h} \frac{h_e^2}{(k+1)^\alpha} \beta \int_e \llbracket \nabla Q_h \cdot \mathbf{n}_e \rrbracket_e \llbracket \nabla w_h \cdot \mathbf{n}_e \rrbracket_e \omega ds \\
 & \quad + \sigma'_{\text{stab}} \sum_{h_e \in \mathcal{E}_h^\partial} \left( h_e [\hat{\mathbf{r}}_2 \cdot \mathbf{n}]_-^2 + \frac{8}{h_e} \right) \int_e Q_h w_h \omega ds \\
 &= \int_{\Gamma_{\text{right}}} \hat{\mathbf{r}}_2 \cdot \mathbf{n} Q_{\text{right}} w_h \omega ds + \sigma'_{\text{stab}} \sum_{h_e \in \mathcal{E}_h^\partial} \left( h_e [\hat{\mathbf{r}}_2 \cdot \mathbf{n}]_-^2 + \frac{8}{h_e} \right) \\
 & \quad \cdot \int_e Q_\partial w_h \omega ds \quad \forall w_h \in \Psi_h. \quad (\text{C2c})
 \end{aligned}$$

The discrete trial and test spaces for the flux-density pair are, for given  $k \geq 0$ , Raviart-Thomas elements of degree  $k$  and overall discontinuous and piecewise polynomials of degree  $k$ , while for the density moment we take overall continuous and piecewise polynomials of degree  $k+1$  (see their precise definition for the Cartesian case in, e.g., Ref. [80] and the

TABLE II. Error history (error decay with respect to the number of degrees of freedom of the product discrete space, and experimental convergence rates) with respect to manufactured smooth solutions using the mixed-primal COIP method with two different polynomial degrees. We also show peak memory usage per mesh refinement (in MB), as well as CPU time (in s).

DoF	$h$	$e(s)$	$r(s)$	$e(P)$	$r(P)$	$e(Q)$	$r(Q)$	Memory	CPU
Lowest-order method with $k = 0$									
33	0.7071	$2.93 \times 10^1$	★	1.03	★	4.92	★	91.55	1.23
113	0.3536	$1.73 \times 10^1$	0.763	$5.56 \times 10^{-1}$	0.888	7.08	-0.526	91.88	1.37
417	0.1768	9.96	0.793	$2.84 \times 10^{-1}$	0.969	1.84	1.943	95.04	1.38
1601	0.0884	5.93	0.747	$1.43 \times 10^{-1}$	0.992	$7.10 \times 10^{-1}$	1.375	10.29	1.41
6273	0.0442	3.72	0.673	$7.16 \times 10^{-2}$	0.997	$3.35 \times 10^{-1}$	1.085	127.33	1.64
24833	0.0221	2.45	0.604	$3.59 \times 10^{-2}$	0.995	$1.63 \times 10^{-1}$	1.036	274.12	3.24
98817	0.0110	1.67	0.551	$1.82 \times 10^{-2}$	0.981	$8.13 \times 10^{-2}$	1.004	730.17	9.21
Scheme with $k = 1$									
97	0.7071	$1.25 \times 10^1$	★	$1.92 \times 10^{-1}$	★	3.60	★	91.92	1.78
353	0.3536	4.35	1.522	$7.00 \times 10^{-2}$	1.456	1.10	1.717	94.76	1.64
1345	0.1768	1.41	1.625	$1.86 \times 10^{-2}$	1.916	$1.81 \times 10^{-1}$	2.602	110.09	1.75
5249	0.0884	$4.79 \times 10^{-1}$	1.557	$4.70 \times 10^{-3}$	1.981	$4.79 \times 10^{-2}$	1.914	149.36	1.87
20737	0.0442	$1.74 \times 10^{-1}$	1.457	$1.18 \times 10^{-3}$	1.995	$1.26 \times 10^{-2}$	1.929	299.89	3.10
82433	0.0221	$6.84 \times 10^{-2}$	1.350	$2.95 \times 10^{-4}$	1.999	$3.21 \times 10^{-3}$	1.972	984.45	8.05
328705	0.0110	$2.89 \times 10^{-2}$	1.245	$7.38 \times 10^{-5}$	2.000	$8.07 \times 10^{-4}$	1.990	3673.87	34.44

modification for axisymmetric divergence in Ref. [81], see also Refs. [82,83]):

$$\Sigma_h := \{\tau_h \in \mathbf{H}(\text{div}_r; \Omega_{\text{FE}}) : \tau_h|_K \in \mathbb{RT}_k(K) \forall K \in \mathcal{T}_h, \tau_h \cdot \mathbf{n}|_{\Gamma_{\text{left}}} = s_{\text{left}}\}, \quad (\text{C3a})$$

$$\Sigma_h^0 := \{\tau_h \in \mathbf{H}(\text{div}_r; \Omega_{\text{FE}}) : \tau_h|_K \in \mathbb{RT}_k(K) \forall K \in \mathcal{T}_h, \tau_h \cdot \mathbf{n}|_{\Gamma_{\text{left}}} = 0\}, \quad (\text{C3b})$$

$$\Phi_h := \{v_h \in L_\omega^2(\Omega_{\text{FE}}) : v_h|_K \in \mathbb{P}_k(K) \forall K \in \mathcal{T}_h\}, \quad (\text{C3c})$$

$$\Psi_h := \{w_h \in C^0(\overline{\Omega_{\text{FE}}}) : w_h|_K \in \mathbb{P}_{k+1}(K) \forall K \in \mathcal{T}_h\}. \quad (\text{C3d})$$

Here by  $\mathbf{H}(\text{div}_r; \Omega_{\text{FE}})$  we mean all vector fields in  $\mathbf{L}_\omega^2(\Omega_{\text{FE}})$  such that their *radial* divergence (3.6) is in the scalar version of the space,  $L_\omega^2(\Omega_{\text{FE}})$ . In turn, for all  $p > 1$ , by  $L_\omega^p(\Omega_{\text{FE}})$  we denote the weighted Lebesgue space of all measurable functions  $v$  on  $\Omega_{\text{FE}}$  such that (see Ref. [84])

$$\|v\|_{L_\omega^p(\Omega_{\text{FE}})}^p := \int_{\Omega_{\text{FE}}} |v|^p \omega \, dr_2 \, dr_1 < \infty.$$

Observe that in the discrete weak formulation we have tested the constitutive equation for the flux against a weighted test function  $D\tau_h$  in order to obtain a block-symmetric structure in the weighted divergence operator. Note also, that since the equation for  $Q_h$  is hyperbolic in nature, we employ a continuous interior penalty (COIP) approach adopted from Ref. [85], that restores the otherwise suboptimal convergence expected when using the space  $\Psi_h$ . This method includes an additional integration by parts [that we conduct using the modified form (C1)] and the interior jump penalization associated with the normal gradients. Other possible choices are classical streamline upwind Petrov-Galerkin or streamline diffusion variants. More details can be found in, e.g., Refs. [85,86].

We confirm experimentally the convergence of (1.1) to the unique weak solution of (3.4) by using smooth manufactured solutions  $P(r_1, r_2) = \sin(\pi r_2) \sin(\pi r_1)$ ,  $Q(r_1, r_2) = \frac{3}{2} + \cos(\pi r_1 r_2)$ , and considering a manufactured right-hand side for the second and third equations of (3.4). We impose natural boundary conditions for  $P_h$  on the right, bottom, and top parts of the boundary, essential boundary conditions for the flux on  $\Gamma_{\text{left}}$  and natural boundary conditions for  $Q_h$  on the boundary  $\Gamma_{\text{right}}$  (the prescribed boundary values and source terms are not necessarily homogeneous but given by the manufactured exact density and density moment). We impose the latter conditions naturally since the upstream mechanism does not permit us to set up a boundary condition essentially on the right boundary (as this can be considered an outflow segment on which  $\hat{\mathbf{r}}_2 \cdot \mathbf{n} > 0$ ). This explains the additional terms on  $\mathcal{E}_h^\partial$  suggested in Ref. [87]. A sequence of successively refined meshes is constructed, and on each level the approximate solutions are compared to the exact ones using the natural norms

$$e(s) := \|s - s_h\|_{\mathbf{H}(\text{div}_r; \Omega_{\text{FE}})}, \quad e(P) := \|P - P_h\|_{L_\omega^2(\Omega_{\text{FE}})}, \\ e(Q) := \|Q - Q_h\|_{H_\omega(\Omega_{\text{FE}})},$$

and experimental convergence rates are computed as  $r_{l+1}(\cdot) = \log(e_{l+1}(\cdot)/e_l(\cdot))[\log(h_{l+1}/h_l)]^{-1}$ , where  $e_l$  denotes the error incurred at the refinement level with a mesh of size  $h_l$ . Here

$$\|\bullet\|_{H_\omega(\Omega_{\text{FE}})}^2 = \|\bullet\|_{L_\omega^2(\Omega_{\text{FE}})}^2 + \int_{\Omega_{\text{FE}}} |\hat{\mathbf{r}}_2 \cdot \nabla(\bullet)|^2 \omega \, dr_2 \, dr_1$$

is the norm in the graph space. The constants are taken as  $\hat{D}_1 = 2$ ,  $\hat{D}_2 = 1.5$ , and we test the schemes with polynomial degrees  $k = 0$  and  $k = 1$ . The numerical parameters associated with the COIP discretization (1.4) are taken as  $\alpha = \frac{7}{2}$ ,  $\beta = 1$ ,  $\sigma_{\text{stab}} = 0.1$ , and  $\sigma'_{\text{stab}} = k + 1$ . The results are presented in Table II, exhibiting optimal convergence for the density  $O(h^{k+1})$ , while the flux shows a suboptimal

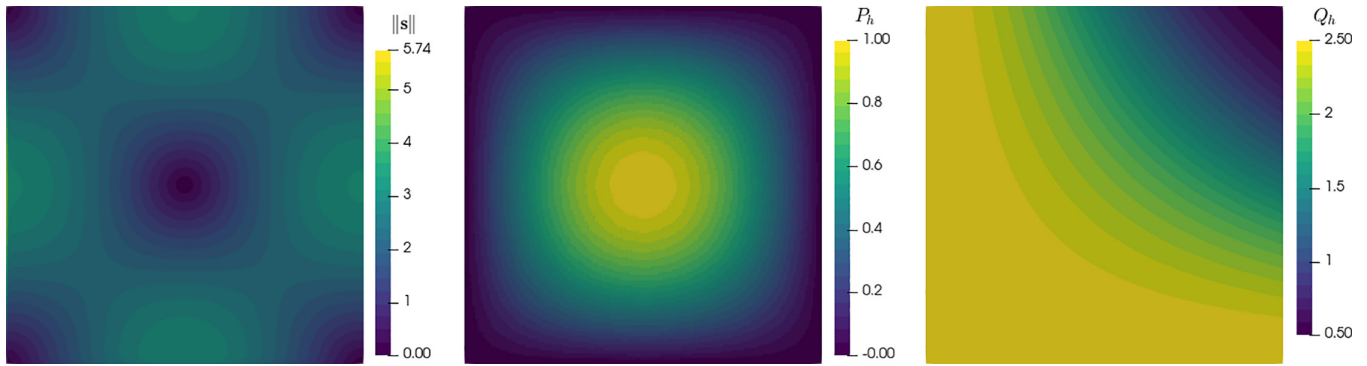


FIG. 11. Approximate solutions for the convergence test, computed with the lowest-order finite-element scheme and shown on a coarse mesh.

error decay at  $O(h^{k+1/2})$  (a suboptimal convergence has been shown theoretically in Ref. [83] for axisymmetric Darcy equations approximated by lowest-order Raviart-Thomas elements). All unknowns exhibit an optimal convergence (in the sense that this is the approximability property of the chosen finite-element spaces). We also report on the required CPU time and peak memory usage per each mesh refinement. Other tests (not shown here) confirm that if we do not use

the COIP strategy, while for the lowest-order case the density moment has optimal convergence, for the case  $k = 1$  we obtain only a  $O(h)$  convergence. We also plot the components of the approximate solution in Fig. 11. For this test, for every mesh refinement and polynomial degree the Newton-Raphson algorithm used for the nonlinear system has taken no more than four iterations to achieve the desired convergence criterion.

- 
- [1] M. H. Jacobs, Diffusion processes, in *Diffusion Processes* (Springer, Berlin, 1935), pp. 1–145.
  - [2] S. S. Mogre, A. I. Brown, and E. F. Koslover, Getting around the cell: Physical transport in the intracellular world, *Phys. Biol.* **17**, 061003 (2020).
  - [3] A. L. Koch, Diffusion the crucial process in many aspects of the biology of bacteria, in *Advances in Microbial Ecology* (Springer US, Boston, MA, 1990), pp. 37–70.
  - [4] D. P. Jones, Intracellular diffusion gradients of  $O_2$  and ATP, *Am. J. Physiol. Cell Physiol.* **250**, C663 (1986).
  - [5] S. T. Kinsey, B. R. Locke, and R. M. Dillaman, Molecules in motion: Influences of diffusion on metabolic structure and function in skeletal muscle, *J. Exp. Biol.* **214**, 263 (2011).
  - [6] B. N. Kholodenko and W. Kolch, Giving space to cell signaling, *Cell* **133**, 566 (2008).
  - [7] F. Ye, D. K. Breslow, E. F. Koslover, A. J. Spakowitz, W. J. Nelson, and M. V. Nachury, Single molecule imaging reveals a major role for diffusion in the exploration of ciliary space by signaling receptors, *Elife* **2**, e00654 (2013).
  - [8] R. J. McMurtrey, Roles of diffusion dynamics in stem cell signaling and three-dimensional tissue development, *Stem Cells Dev.* **26**, 1293 (2017).
  - [9] A. M. North, Diffusion-controlled reactions, *Q. Rev. Chem. Soc.* **20**, 421 (1966).
  - [10] B. Alberts, A. Johnson, J. Lewis, D. Morgan, and M. Raff, *Molecular Biology of the Cell* (Taylor & Francis, Oxford, UK, 2014).
  - [11] J. D. Murray, *Mathematical Biology: v I. An Introduction* (Springer Science & Business Media, New York, 2007), Vol. 17, p. 175.
  - [12] W. W. Chen, M. Niepel, and P. K. Sorger, Classic and contemporary approaches to modeling biochemical reactions, *Genes Dev.* **24**, 1861 (2010).
  - [13] S. Soh, M. Byrská, K. Kandere-Grzybowska, and B. A. Grzybowski, Reaction-diffusion systems in intracellular molecular transport and control, *Angew. Chem. Int. Ed.* **49**, 4170 (2010).
  - [14] S. Kondo and T. Miura, Reaction-diffusion model as a framework for understanding biological pattern formation, *Science* **329**, 1616 (2010).
  - [15] P. C. Bressloff, *Stochastic Processes in Cell Biology* (Springer, Berlin, 2022), Vol. 41.
  - [16] H. H. McAdams and A. Arkin, It's a noisy business! Genetic regulation at the nanomolar scale, *Trends Genet.* **15**, 65 (1999).
  - [17] R. Losick and C. Desplan, Stochasticity and cell fate, *Science* **320**, 65 (2008).
  - [18] E. Roberts, A. Magis, J. O. Ortiz, W. Baumeister, and Z. Luthey-Schulten, Noise contributions in an inducible genetic switch: A whole-cell simulation study, *PLoS Comput. Biol.* **7**, 1 (2011).
  - [19] P. J. Halling, Do the laws of chemistry apply to living cells? *Trends Biochem. Sci.* **14**, 317 (1989).
  - [20] R. Erban and S. J. Chapman, Stochastic modelling of reaction-diffusion processes: Algorithms for bimolecular reactions, *Phys. Biol.* **6**, 046001 (2009).
  - [21] S. Smith and R. Grima, Spatial stochastic intracellular kinetics: A review of modelling approaches, *Bull. Math. Biol.* **81**, 2960 (2019).
  - [22] D. T. Gillespie, A rigorous derivation of the chemical master equation, *Physica A* **188**, 404 (1992).
  - [23] T. Turner, S. Schnell, and K. Burrage, Stochastic approaches for modelling in vivo reactions, *Comput. Biol. Chem.* **28**, 165 (2004).
  - [24] T. Jahnke and W. Huisinga, Solving the chemical master equation for monomolecular reaction systems analytically, *J. Math. Biol.* **54**, 1 (2006).



- [25] D. T. Gillespie, A general method for numerically simulating the stochastic time evolution of coupled chemical reactions, *J. Comput. Phys.* **22**, 403 (1976).
- [26] D. T. Gillespie, Exact stochastic simulation of coupled chemical reactions, *J. Phys. Chem.* **81**, 2340 (1977).
- [27] D. Bernstein, Simulating mesoscopic reaction-diffusion systems using the Gillespie algorithm, *Phys. Rev. E* **71**, 041103 (2005).
- [28] S. Lampoudi, D. T. Gillespie, and L. R. Petzold, The multinomial simulation algorithm for discrete stochastic simulation of reaction-diffusion systems, *J. Chem. Phys.* **130**, 094104 (2009).
- [29] S. A. Isaacson, The reaction-diffusion master equation as an asymptotic approximation of diffusion to a small target, *SIAM J. Appl. Math.* **70**, 77 (2009).
- [30] M. Malek-Mansour and J. Houard, A new approximation scheme for the study of fluctuations in nonuniform nonequilibrium systems, *Phys. Lett. A* **70**, 366 (1979).
- [31] J. Elf and M. Ehrenberg, Spontaneous separation of bi-stable biochemical systems into spatial domains of opposite phases, *Syst. Biol.* **1**, 230 (2004).
- [32] J. Hattne, D. Fange, and J. Elf, Stochastic reaction-diffusion simulation with MesoRD, *Bioinformatics* **21**, 2923 (2005).
- [33] S. Engblom, L. Ferm, A. Hellander, and P. Lötstedt, Simulation of stochastic reaction-diffusion processes on unstructured meshes, *SIAM J. Sci. Comput.* **31**, 1774 (2009).
- [34] I. Hepburn, W. Chen, S. Wils, and E. De Schutter, STEPS: efficient simulation of stochastic reaction-diffusion models in realistic morphologies, *BMC Syst. Biol.* **6**, 36 (2012).
- [35] S. A. Isaacson, A convergent reaction-diffusion master equation, *J. Chem. Phys.* **139**, 054101 (2013).
- [36] A. Hospital, J. R. Goñi, M. Orozco, and J. L. Gelpí, Molecular dynamics simulations: Advances and applications, *Adv. Appl. Bioinf. Chem.* **8**, 37 (2015).
- [37] M. Orozco, L. Orellana, A. Hospital, A. N. Naganathan, A. Emperador, O. Carrillo, and J. Gelpí, Coarse-grained representation of protein flexibility. Foundations, successes, and shortcomings, in *Computational Chemistry Methods in Structural Biology*, Advances in Protein Chemistry and Structural Biology, Vol. 85, edited by C. Christov (Academic Press, San Diego, CA, 2011), pp. 183–215.
- [38] M. Feig and Y. Sugita, Whole-cell models and simulations in molecular detail, *Annu. Rev. Cell Dev. Biol.* **35**, 191 (2019).
- [39] J. Schöneberg, A. Ullrich, and F. Noé, Simulation tools for particle-based reaction-diffusion dynamics in continuous space, *BMC Biophys.* **7**, 1 (2014).
- [40] M. V. Smoluchowski, Versuch einer mathematischen theorie der koagulationskinetik kolloider lösungen, *Z. Phys. Chem.* **92**, 129 (1917).
- [41] J. S. van Zon and P. R. ten Wolde, Simulating biochemical networks at the particle level and in time and space: Green's function reaction dynamics, *Phys. Rev. Lett.* **94**, 128103 (2005).
- [42] J. S. van Zon and P. R. ten Wolde, Green's-function reaction dynamics: A particle-based approach for simulating biochemical networks in time and space, *J. Chem. Phys.* **123**, 234910 (2005).
- [43] K. Takahashi, S. Tănase-Nicola, and P. R. ten Wolde, Spatio-temporal correlations can drastically change the response of a MAPK pathway, *Proc. Natl. Acad. Sci. USA* **107**, 2473 (2010).
- [44] T. R. Sokolowski, J. Paijmans, L. Bossen, T. Miedema, M. Wehrens, N. B. Becker, K. Kaizu, K. Takahashi, M. Dogterom, and P. R. ten Wolde, eGFRD in all dimensions, *J. Chem. Phys.* **150**, 054108 (2019).
- [45] S. S. Andrews and D. Bray, Stochastic simulation of chemical reactions with spatial resolution and single molecule detail, *Phys. Biol.* **1**, 137 (2004).
- [46] J. Schöneberg and F. Noé, Readdy—A software for particle-based reaction-diffusion dynamics in crowded cellular environments, *PLoS ONE* **8**, e74261 (2013).
- [47] S. A. Rice, Chapter 2 diffusion-controlled reactions in solution, in *Diffusion-Limited Reactions*, Comprehensive Chemical Kinetics, Vol. 25, edited by C. Bamford, C. Tipper, and R. Compton (Elsevier, Amsterdam, 1985), pp. 3–46.
- [48] F. C. Collins and G. E. Kimball, Diffusion-controlled reaction rates, *J. Colloid Sci.* **4**, 425 (1949).
- [49] M. Doi, Stochastic theory of diffusion-controlled reaction, *J. Phys. A: Math. Gen.* **9**, 1479 (1976).
- [50] T. Kearney and M. B. Flegg, Enzyme kinetics simulation at the scale of individual particles, *J. Chem. Phys.* **161**, 194111 (2024).
- [51] M. B. Flegg, Smoluchowski reaction kinetics for reactions of any order, *SIAM J. Appl. Math.* **76**, 1403 (2016).
- [52] S. Redner and D. ben Avraham, Nearest-neighbour distances of diffusing particles from a single trap, *J. Phys. A: Math. Gen.* **23**, L1169 (1990).
- [53] S. Chandrasekhar, Stochastic problems in physics and astronomy, *Rev. Mod. Phys.* **15**, 1 (1943).
- [54] Z. Koza, T. Yanir, and H. Taitelbaum, Nearest-neighbor distance at a single mobile trap, *Phys. Rev. E* **58**, 6821 (1998).
- [55] A. D. Sánchez, M. A. Rodríguez, and H. S. Wio, Results in trapping reactions for mobile particles and a single trap, *Phys. Rev. E* **57**, 6390 (1998).
- [56] K. Kang and S. Redner, Scaling approach for the kinetics of recombination processes, *Phys. Rev. Lett.* **52**, 955 (1984).
- [57] F. Leyvraz and S. Redner, Spatial structure in diffusion-limited two-species annihilation, *Phys. Rev. A* **46**, 3132 (1992).
- [58] A. Donev, J. Rockwell, and D. Ben-Avraham, Generalized von Smoluchowski model of reaction rates, with reacting particles and a mobile trap, *J. Stat. Phys.* **95**, 97 (1999).
- [59] M. K. Kadalbajoo and K. C. Patidar, Singularly perturbed problems in partial differential equations: A survey, *Appl. Math. Comput.* **134**, 371 (2003).
- [60] J. C. Neu, *Singular Perturbation in the Physical Sciences*, Vol. 167 (American Mathematical Society, Providence, RI, 2015).
- [61] H.-G. Roos, H.-G. Roos, M. M. Stynes, and L. L. Tobiska, *Robust Numerical Methods for Singularly Perturbed Differential Equations: Convection-Diffusion-Reaction and Flow Problems*, 2nd ed., Springer Series in Computational Mathematics, Vol. 24 (Springer, Berlin, 2008), pp. 235–421.
- [62] R. Lin and M. Stynes, A balanced finite element method for singularly perturbed reaction-diffusion problems, *SIAM J. Numer. Anal.* **50**, 2729 (2012).
- [63] K. Khari and V. Kumar, An efficient numerical technique for solving nonlinear singularly perturbed reaction diffusion problem, *J. Math. Chem.* **60**, 1356 (2022).
- [64] D. L. Ermak and J. A. McCammon, Brownian dynamics with hydrodynamic interactions, *J. Chem. Phys.* **69**, 1352 (1978).
- [65] A. L. Edelstein and N. Agmon, Brownian dynamics simulations of reversible reactions in one dimension, *J. Chem. Phys.* **99**, 5396 (1993).

- [66] J. Lipková, K. C. Zygalakis, S. J. Chapman, and R. Erban, Analysis of Brownian dynamics simulations of reversible bi-molecular reactions, *SIAM J. Appl. Math.* **71**, 714 (2011).
- [67] H. Schlichting (Deceased) and K. Gersten, Fundamentals of boundary-layer theory, in *Boundary-Layer Theory* (Springer, Berlin, 2017), pp. 29–49.
- [68] R. Becker, D. Capatina, and R. Luce, Local flux reconstructions for standard finite element methods on triangular meshes, *SIAM J. Numer. Anal.* **54**, 2684 (2016).
- [69] G. N. Gatica, A simple introduction to the mixed finite element method, in *Theory and Applications. Springer Briefs in Mathematics* (Springer, London, 2014).
- [70] D. Angeli, J. E. Ferrell, and E. D. Sontag, Detection of multistability, bifurcations, and hysteresis in a large class of biological positive-feedback systems, *Proc. Natl. Acad. Sci. USA* **101**, 1822 (2004).
- [71] T. Wilhelm, The smallest chemical reaction system with bistability, *BMC Syst. Biol.* **3**, 90 (2009).
- [72] M. A. Branch, T. F. Coleman, and Y. Li, A subspace, interior, and conjugate gradient method for large-scale bound-constrained minimization problems, *SIAM J. Sci. Comput.* **21**, 1 (1999).
- [73] P. Virtanen, R. Gommers, T. E. Oliphant, M. Haberland, T. Reddy, D. Cournapeau, E. Burovski, P. Peterson, W. Weckesser, J. Bright, S. J. van der Walt, M. Brett, J. Wilson, K. J. Millman, N. Mayorov, A. R. J. Nelson, E. Jones, R. Kern, E. Larson, C. J. Carey *et al.*, Scipy 1.0: Fundamental algorithms for scientific computing in python, *Nat. Methods* **17**, 261 (2020).
- [74] R. Erban, J. Chapman, and P. Maini, A practical guide to stochastic simulations of reaction-diffusion processes, [arXiv:0704.1908](https://arxiv.org/abs/0704.1908).
- [75] A. Goldbeter, Oscillatory enzyme reactions and Michaelis-Menten kinetics, *FEBS Lett.* **587**, 2778 (2013).
- [76] H. Shankaran and H. S. Wiley, Oscillatory dynamics of the extracellular signal-regulated kinase pathway, *Curr. Opin. Genet. Dev.* **20**, 650 (2010).
- [77] P. Kraikivski, Glycolytic oscillations, in *Case Studies in Systems Biology* (Springer International Publishing, Cham, 2021), pp. 59–68.
- [78] M. S. Alnæs, J. Blechta, J. Hake, A. Johansson, B. Kehlet, A. Logg, C. Richardson, J. Ring, M. E. Rognes, and G. N. Wells, The FEniCS Project Version 1.5, *Arch. Numer. Softw.* **3**, 9 (2015).
- [79] <https://github.com/ruizbaier/closestMolecule>.
- [80] A. Ern and J.-L. Guermond, *Theory and Practice of Finite Elements*, Applied Mathematical Sciences Vol. 159 (Springer-Verlag, New York, 2004), pp. 3–80.
- [81] V. Ervin, Approximation of axisymmetric Darcy flow using mixed finite element methods, *SIAM J. Numer. Anal.* **51**, 1421 (2013).
- [82] G. Baird, R. Bürger, P. E. Méndez, and R. Ruiz-Baier, Second-order schemes for axisymmetric Navier–Stokes–Brinkman and transport equations modelling water filters, *Numer. Math.* **147**, 431 (2021).
- [83] M. Neilan and A. Zytoon, Low-order Raviart–Thomas approximations of axisymmetric Darcy flow, *J. Math. Anal. Appl.* **473**, 905 (2019).
- [84] C. Bernardi, M. Dauge, Y. Maday, and M. Azaiez, *Spectral Methods for Axisymmetric Domains, Series in Applied Mathematics* (Gauthier–Villars & North-Holland, Elsevier, Paris, 1999).
- [85] E. Burman and A. Ern, Continuous interior penalty *hp*-finite element methods for advection and advection-diffusion equations, *Math. Comput.* **76**, 1119 (2007).
- [86] P. B. Bochev, M. D. Gunzburger, and J. N. Shadid, Stability of the SUPG finite element method for transient advection–diffusion problems, *Comput. Methods Appl. Mech. Eng.* **193**, 2301 (2004).
- [87] E. Burman and C. He, Primal dual mixed finite element methods for indefinite advection-diffusion equations, *SIAM J. Numer. Anal.* **57**, 2785 (2019).